POLITECNICO DI MILANO
SCHOOL OF INDUSTRIAL AND INFORMATION ENGINEERING
MATERIALS ENGINEERING AND NANOTECHNOLOGY

Synthesis and characterization of cobalt ferrite – barium titanate magnetoelectric nanoparticles used in neuromodulation systems

Laurea Magistrale – equivalent to Master of Science

Student: Aleksandra Milojkovic

Academic year 2020/2021

Supervisors:

1. Dr. Kristen L. Kozielski, Karlsruhe Institute of Technology
2. Dr. Luca Giampaolo Nobili, Politecnico di Milano

Abstract:

In the past decades, neuromodulation showed a huge potential to be used for therapeutic purposes. This master thesis is based on a research about magnetoelectric composite nanoparticles based on barium titanate and cobalt ferrite that exert a possibility to be used in the deep brain stimulation management. Magnetoelectric coupling is achieved by the strain coupling between ferroelectric component (barium titanate) and ferromagnetic component (cobalt ferrite). Furthermore, this master thesis is divided into five main sections. In the first section, an idea and motivation for this research are given. Also, basic principles of neuromodulation are briefly explained. The second section is dedicated to the full theoretical description of the mentioned effects (magnetoelectric effect, ferroelectric effect and ferromagnetic effect), properties and structure of the chosen materials. This section is finalized with basic principles and protocols of the used methods to characterize the obtained powders. The experimental part fully describes the sol gel technique that is used to obtain these magnetoelectric nanoparticles. After the experimental part, results obtained from the characterization of the nanopowders are given and explained. More precisely, they are characterized by SEM, TEM, XRD, FTIR and AGM. Since these powders have a possibility to be injected in the human brain, it was necessary to perform toxicity measurements. Finally, this master thesis is finalized with conclusions.

Outline:

List of figures:

List of tables:

1. Introduction

Neuromodulation – basic principles

In the past decades, neuromodulation devices have been widely researched and implanted in the human bodies and many therapeutic benefits have been achieved by them.

Neuromodulation is based on a direct act on neuron activity by delivering electrical or pharmaceutical agents to the target area. The most common application of the neuromodulation process is the pain relief. However, this method can also be used in deep brain stimulation (DBS) that is used for treatment of Parkinson disease. [1] Devices that electrically modulate the deep brain induce a possibility of harvesting electrical signal in the human body. The main issue of them is that they require a surgical implantation and they are on the centimeter scale. Other than that, they can also carry the risk of hemorrhage and infection, thus being highly invasive. [2]

The scope of this research is the synthesis and characterization of the injectable magnetoelectricnanoelectrodes for DBS. These electrodes wirelessly transmit electrical signals to the neurons by the application of the magnetic field making them a promising substitution of electrical modulation devices. Wireless transmission would definitely lead to less invasive neurostimulation and no genetic modifications will occur. This mechanism of neurostimulation is successfully managed by injection of the nanoelectrodes into the mouse brain which lead to local subthalamic modulation that promotes behavioral changes in mice. [2] The main idea was to synthesize composite nanoparticles where barium titanate is a ferroelectric component and cobalt ferrite ferromagnetic component. By strain coupling of these two phases, magnetoelectric effect will be exhibited. More precisely, by the application of the external magnetic field, strain will be generated in the ferromagnetic phase ($CoFe_2O_4$) that as a result will induce strain in the ferroelectric ($BaTiO_3$) and charge separation will occur. As a result, wireless neurostimulationis achieved.
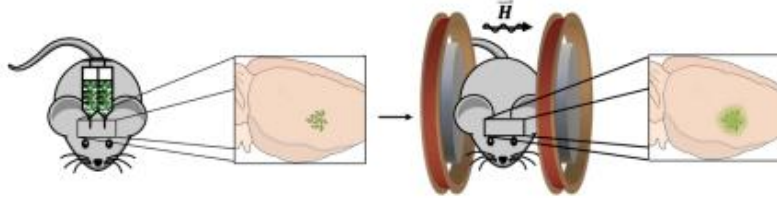
Figure 1. MEN electrodes injected in the subthalamic region causing a movement, [2]

2. Theoretical part:

Firstly, some theoretical basis of magenotelectric effect, piezoelectricity and magnetostriction is given. Later on, basic principles of the used methods to characterize the obtained nanoelectrodes are also explained. On top of that, a brief protocol of the each used method is shown.

2.1 Magnetoelectric effect in composites

In this section, magnetoelectric effect in composites is mathematically and phenomenologically described. Magnetoelectric effect (ME) stands for any kind of coupling between the magnetic and electric properties. In other words, magnetoelectric effect modifies the electronic state of the crystal which results in the change of the net magnetic moment. Magnetoelectric materials can be electrically polarized by a magnetic field or conversely, magnetized by an electrical field. This effect can be described as follows:

$$Pi = \propto ijHj$$

$$Mi = \frac{\propto ji}{\mu 0} Ej$$

Where μ0 is a permeability of the free space; Pi polarization due to the applied magnetic field Hj; Mi magnetization due to the applied electrical field Ej; αji stands for the magnetic susceptibility and in this case it is a second order tensor.

Coupling of the piezoelectric and magnetostrictive component is occurring at the interface and it can be mathematically described by an interfacial coupling factor k. To exert a perfect magnetoelectric coupling, k should be equal to 1. **[3]**

In this research, of particular interest are magnetoelectric materials on the nano scale where high density of interfaces will potentially induce an enhanced ME effect. **[4]** Various types of

piezoelectric and piezomagnetic materials are used in order to achieve an excellent magnetoelectric effect. In this work, as a ferroelectric component, barium titanate was chosen due to its excellent piezoelectric properties and environmental friendliness. As a magnetic component, cobalt ferrite was a chosen material. The reason behind this is its strong magnetostriction. Great advantage of these composites is spinodal decomposition at high temperatures that prevents interactions among them during processing. **[4]** To have a better assessment of the magnetoelectric effect, it is necessary to describe piezoelectricity and magnetostriction.

2.2 Piezoelectricity and ferroelectric materials

Piezoelectricity is a conversion of a mechanical input into an electrical output or vice versa. In direct piezoelectric effect, mechanical input is converted into an electrical one. Conversely, in converse piezoelectric effect, electrical signal is converted into a mechanical output.

A very important property of the piezoelectricity is reversibility meaning that materials exhibiting a direct piezoelectric effect also exhibit a converse piezoelectric effect.

By default, an unstressed material exerts no electrical output as positive and negative charges will be balanced out. By applying the stress, positions of the charges will be displaced with respect to each other and deformation will occur. As a result, charges will not cancel each other as the material will tend to form positive charges on one side and negative charges on the other side, hence dipoles. This build up potential difference will enable charges to produce electricity.

Not all materials can be poled by piezoelectricity. In the absence of an electric field, piezoelectric domains will be randomly oriented, hence no polarization occurs. When electric field is applied, domains will tend to align in the poling direction and charge separation will be induced creating dipoles. When the electric field is switched off, most of the dipoles will stay aligned due to the pinning effect that comes out as a result of the produced microscopic defects. Needless to say, material can also be de-poled when subjected to an electrical field of the opposite sign or being exposed to higher temperatures than the Curie temperature.
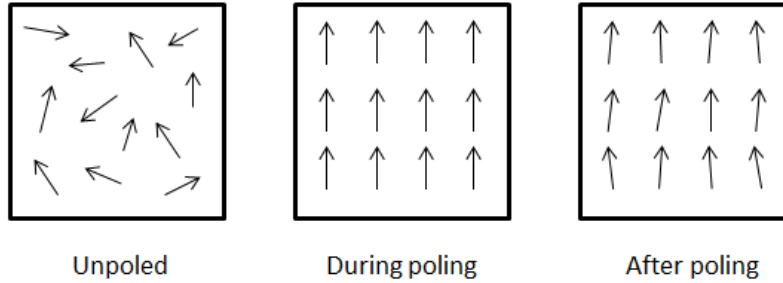
Figure 2. Piezoelectric poling process scheme, [5]

Piezoelectricity occurs even naturally in some materials. Quartz (SiO_2) is the first naturally occuring piezoelectric material that is characterized by a continuous network of SiO_4 tetrahedrals. Some other non crystalline materials show a natural piezoelectric effect. Some examples are bones, enamel, dentin. However, the degree of piezoelectric effect in naturally occuring materials is considered to be low. Artificially made piezoelectric materials exhibit piezoelectric effect that is even 100 times higher than in the naturally occuring materials. **[6]**

For a material to exhibit the poling process, it must be characterized by an absence of the center of symmetry. The most widely researched non centrosymmetric piezoelectric materials have perovskite structure with the general formula of ABO_3. Moreover, perovskite structure materials are constituted by tetravalent ions (B) placed within a lattice of divalent ions (A) and oxygen ions.

Piezoelectric poling strongly depends on temperature. A fundamental piezoelectric property is a Curie temperature, which stands for a limit of the poling process. More precisely, poling can only be exerted below this temperature. Above the Curie temperature, as previously denoted, de-poling is achieved.
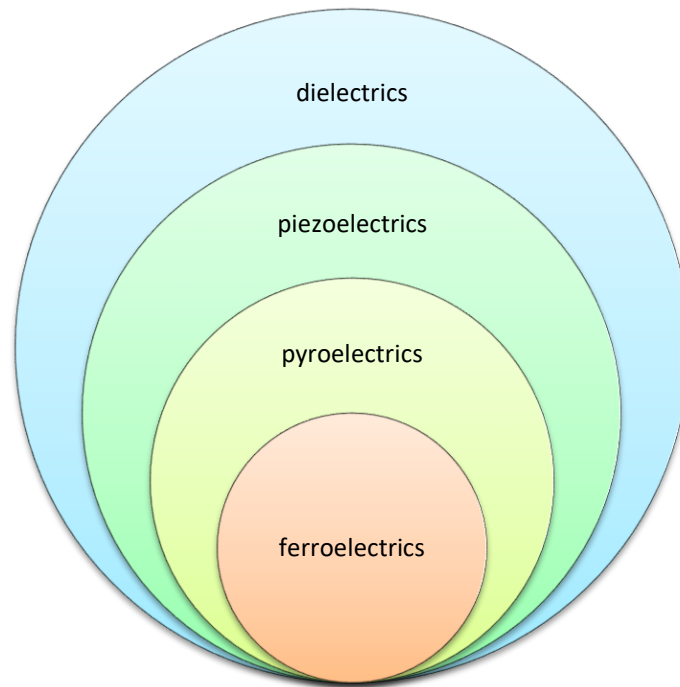
Figure 3. Schematic representation of different types of electrics

Ferroelectric materials belong to the class of piezoelectric materials (figure 3) and they can be defined as materials having spontaneous polarization below the Curie temperature even in the absence of the electrical field. The change occurring at the Curie temperature will not only produce a mechanical strain, but also change in the refractive index.

Additionally, ferroelectric materials are characterized by piezoelectric, pyroelectric[1] and electro-optic effects. Also, the polarity of ferroelectric materials can be completely reversed by applying an opposite electrical field.

However, the spontaneous polarization in the ferroelectric materials is not completely uniformly aligned throughout the same direction. That's why the ferroelectric crystal can be thought as a collection of regions having an equal spontaneous polarization. These regions are better called ferroelectric domains and they are separated by the ferroelectric walls, which gradually change the direction of the spontaneous polarization. **[7]** Two different types of walls can be distinguished. The ones that separate domains having opposite polarization are called 180⁰ walls. Others are called 90⁰ walls and they separate mutually perpendicular polarized regions. The reason behind the domain formation is that they minimize the depolarizing fields and the elastic energy that is correlated with mechanical constrains to which ferroelectric material is subjected.

---

[1] Ability of materials to be poled by an act of temperature

In a polarization versus electric field curve, they show a hysteresis loop, hence non-linear response.
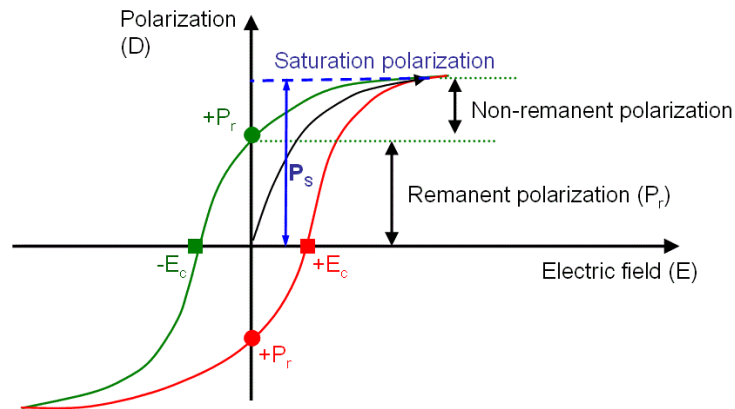
Figure 4. Electric hysteresis loop of ferroelectric materials, [9]

A typical hysteresis loop is show on the figure and key parameters were labeled accordingly.

The poling process is usually performed at elevated temperatures and high values of the electric field (10 – 100 kV/cm). The poling process is only possible in the case of ferroelectric materials and not in the case of non-ferroelectric piezoelectric materials as polarity of these materials cannot be reversed.

Saturation polarization is the maximum induced electric polarization and at this point all the domains are oriented in the poling direction. When the electrical field is switched off, remanent polarization (Pr) can be measured and it is a polarization that remains in the material. Electrical coercivity, Ec, can be defined as a degree of field needed to bring polarization to zero. The negative values –Ec and –Pr are obtained when the field in the other direction is applied. In an ideal case, the loop is symmetric, meaning that positive and negative values of coercivity and remanent polarization are equal. **[8]**

2.3 Magnetostriction and magnetic materials

Magnetostriction is a characteristic of ferromagnetic materials that can be described as a change in dimensions or shape that is caused by an act of the magnetic field. This change of dimension can either be elongation or shrinkage. In other words, magnetostrictive materials convert electromagnetic energy into mechanical energy or vice versa. As the name is already saying, orientations of the magnetic domains will be changed due to the change in dimensions. **[10]** Magnetostriction can be seen in the form of two effects which are direct and Wiedemann effect. **[11]** In the research, the exploited effect is the Wiedemann effect, which is wirelessly induced in a material. The main advantage of this effect is that the higher energy density can be

achieved. At the same time, magnetic materials are less prone to fatigue in comparison with piezoelectrics. **[12]** Since magnetostriction is in the direct correlation with ferromagnetism, all the peculiarities applied on ferromagnetism also stand for magnetostriction. **[13]**

From now on, a term ferromagnetic material will be often used. Ferromagnetic materials are analogue of previously described ferroelectric materials. Nevertheless, to distinguish between different types of magnetic materials, a brief explanation is given in the following text.

Paramagnetic ordering

Antiferromagnetic ordering

Ferromagnetic ordering

Ferrimagnetic ordering
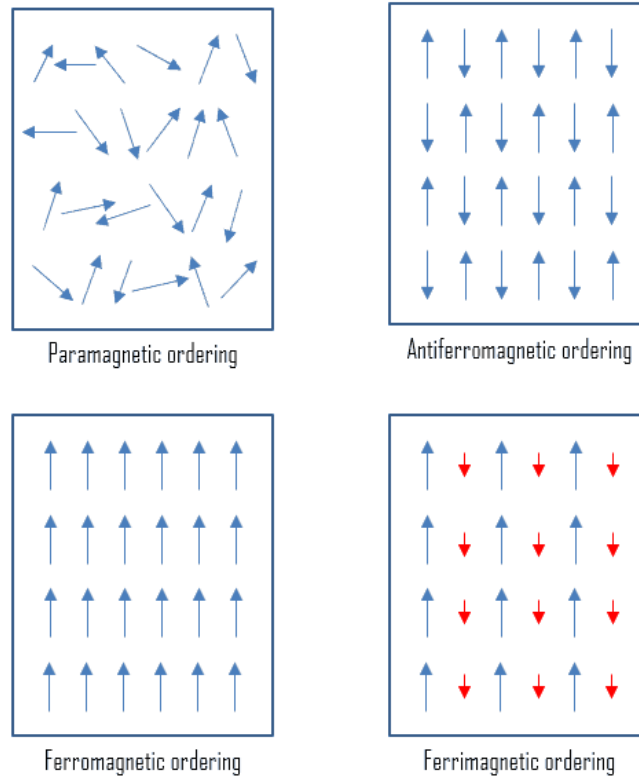
Figure 5. Schematic representation of different kinds of magnetisms, [14]

Firstly, paramagnetic materials are characterized by randomly oriented dipoles which cancel out each other and as a result material is considered as a nonmagnetic material. However, the magnetization occurs only when the external magnetic field is imposed. They are characterized by a magnetic susceptibility higher than 1.

Antiferromagnetic materials spontaneously align themselves at relatively low temperatures into opposite arrangements so that almost zero magnetism is exhibited. Here the opposite moments are equal and they cancel out each other. Antiferromagnetism strongly depends on temperature and it vanished above a certain temperature limit that is called the Neel temperature. Above the Neel temperature, material is most commonly paramagnetic.

Ferromagnetism stands for a permanent magnetism and it is the strongest among the all previously mentioned magnetisms. Materials exhibiting this kind of behavior remain magnetized also when the external magnetic field is removed. They are also dependent on temperature and the limit of ferromagnetism is called the Curie temperature. Above this temperature, ferromagnetic behavior is lost.

Ferrimagnetic materials are also characterized by a spontaneous magnetization which is slightly lower than in the case of the ferromagnetic materials. As denoted on the picture, ferrimagnetic materials are composed by antiparallel domains which are not equal and thus spontaneous magnetization still occurs. Additionally, ferrites are great ferrimagnetic candidates. Among them, cobalt ferrite is the best candidate due to its high Curie temperature and high magnetic anisotropy. **[14]**

By applying the magnetic field to the ferrimagnetic material, its dipoles tend to rotate and align with the field. As a result, this induces a strain in the material.

The structure of ferromagnetic and ferrimagnetic materials can be described as a uniform collection of the magnetic domains. Using the same analogy as for the ferroelectric materials, the interior of ferromagnetic materialscan be thought of as a division of the domains. These domains can be described as small regions having magnetic dipoles oriented in the same direction.
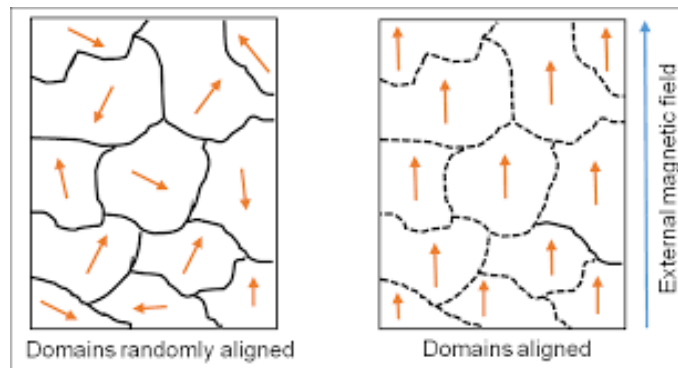
Figure 6. Representation of the ferromagnetic domains, [15]

Domains are divided by Bloch walls that are made of thin layer of atoms in which dipoles are gradually rotated to reach the orientation of the neighboring domain.

When no magnetic field is applied to the ferromagnetic material, dipoles are randomly oriented. When the magnetic field is applied, dipoles will tend to rotate and align with the direction of the external magnetic field. This dipole rotation will induce the strain in the material.

As previously denoted, magnetic anisotropy is characterized by a preferential direction of the magnetization. Furthermore, the direction can be easy or hard. The hard direction shows the most opposition to the imposed magnetic field. For example, in FCC, the dipoles prefer to align along the edge of the cube.

Additionally, the degree of magnetostriction can be described by the magnetostrictive coefficient, λ. Magnetostrictive coefficient stands for the ratio of the strain and the magnetization. This coefficient is applicable up to the magnetization saturation where the material reaches its maximum strain and it cannot be deformed beyond that. Even if the applied magnetic field goes beyond the saturation magnetism, it would not induce any effect in the material because the domains cannot be furthermore aligned. **[16]**

2.4 Magnetic properties – hysteresis loop

This section is focused on describing the magnetic hysteresis loop and the properties that could be assessed from it.

Namely, magnetic hysteresis loop stands for the dependency of the magnetization versus the applied magnetic field. However, not every material can exhibit a magnetic hysteresis loop. Materials showing this kind of behavior are described as non-linear. More precisely, hysteresis loop is obtained when an external magnetic field is applied to the ferromagnetic materials. In order to have a complete overview of the magnetic behavior, linear magnetic behavior will also be briefly explained.

Linear magnetic behavior (dashed line on the Figure 7) stands for a linear dependency of the magnetic field on the magnetic force and the constant of proportionality is given by the magnetic permeability:

$$M = \chi * H$$

Where M stands for magnetization, χ for magnetic susceptibility and H for the external applied field.

Another way to represent the linear behavior:

$$B = \mu * H = \mu 0 * (1 + \chi)H = \mu 0 * (M + H)$$

Where B is the magnetic flux density and it is a direct consequence of the magnetization; μ0 is permeability of the free space.

Magnetic permeability can be defined as an overall change in resultant magnetic field in the material when the external magnetic field is applied. Magnetic permeability can be represented by the following:

$$\mu = \mu 0 * \mu r$$

Where μ_r is a relative magnetic permeability.

Materials having µr equal to 1 are not magnetically responding to the external magnetic field.

Magnetic susceptibility is a degree of the possible magnetization of the material and it is equal to the ratio of magnetization M and magnetic field strength H. **[17]**

Now, moving on to the non-linear behavior, hence ferromagnetic materials.
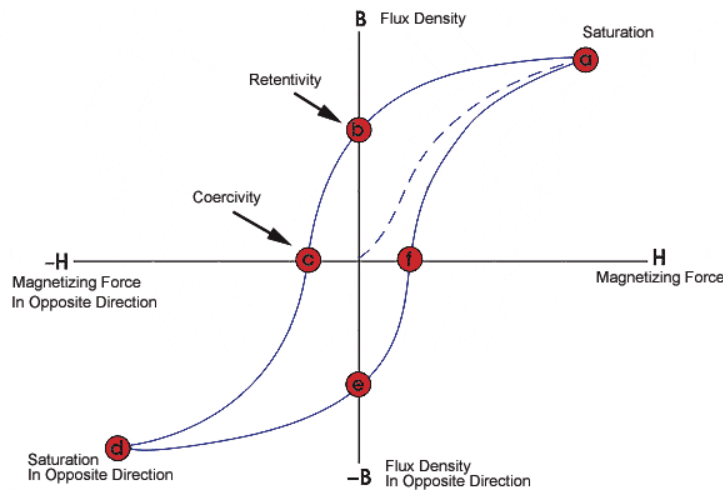
Figure 7. B-H hysteresis loop, [18]

The loop is generated by variation of the magnetic field (H) and measurement of the magnetization in ferromagnetic materials. Direct correlation between the magnetic field and induced magnetization can be noted. Moreover, larger is the applied positive magnetic field (H), larger is the induced magnetization. On the domain scale, this can be described as a dipole alignment. When zero magnetic field is applied, all the domains are randomly oriented and as the field is applied, they tend to align up to a certain limit, which is called the saturation. At saturation, all the domains are oriented in the direction of the magnetic field. Reducing the magnetic field to zero, it can be noticed that the magnetization won't be null. This magnetic property is called retentivity and it denotes the residual magnetism. **[18]**

Imposing the magnetic field in the reverse direction, the point where the flux density is null, is reached. This property is called coercivity and it stands for the amount of force required to remove the residual magnetism.

To summarize, the following magnetic properties can be obtained from the hysteresis loop:

- Retentivity
- Residual magnetism
- Coercivity
- Permeability
- Reluctance[2]

Furthermore, according to the different width of the loop, magnetic materials can be divided into hard and soft magnetic materials. Hard magnetic materials are characterized by a wider hysteresis loop, which is characterized by high retentivity, high residual magnetism, high coercivity, high reluctance and low permeability. Hard magnets are also often called permanent magnets.
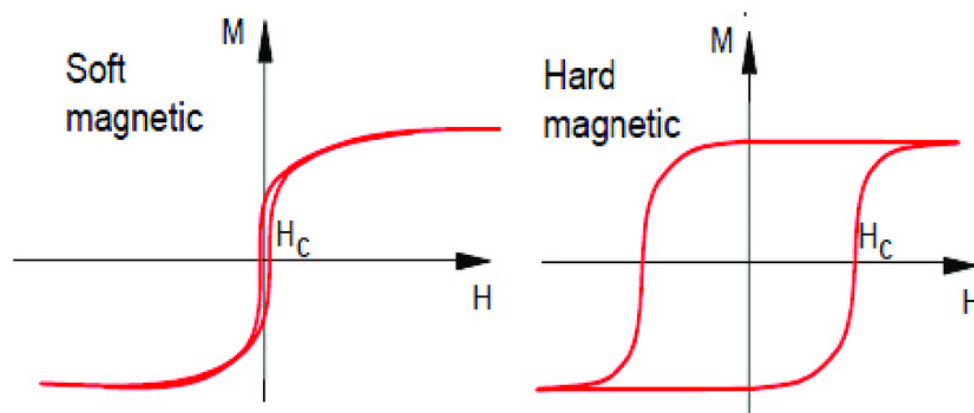
Figure 8. Hysteresis loops of soft magnetic and hard magnetic materials, [19]

Cobalt ferrite is a semi-hard magnetic material that is characterized by high saturation magnetism. In the experimental part, results of the magnetic measurements will be explained. It is expected to obtain a semi-hard magnetic material with intermediate values of coercivity. Magnetic saturation should be as high as possible.

---

[2] Analogue to electrical resistance

2.5 Materials' structure and properties

In this section, firstly individual properties of the chosen materials are described with an accent on their structure. To conclude this section, potential of the magnetoelectric coupling of these materials is described.

Cobalt ferrite

Cobalt ferrite ($CoFe_2O_4$, CFO) is a material that belongs to the group of ferrites with general formula MFe_2O_4. Due to its unique properties, it has found many applications in numerous fields, such as biotechnology, sensors, pigments, catalysts... Among all the ferrites, it has been widely researched in biomedical application due to its highest magnetic anisotropy and magnetic moment. High magnetic anisotropy makes the relaxation of the magnetic moment slower. Also, magnetic anisotropy means that there will always be a preferential direction of the magnetization. These directions usually coincide with the principal axes. Generally speaking, all ferromagnetic materials are characterized by the magnetic anisotropy.

On top of that, CFO is characterized by a great chemical and thermal stability. Another great advantage of it is that it can be synthesized by many different methods.

Cobalt ferrite is characterized by the inverse spinel structure with the face centered cubic lattice. It belongs to the group of spinel ferrites, $MFeO_4$ (where M stands for metal, which in this case is cobalt). Spinel structure can be described as a cubic closely packed arrangement of oxygen atoms. Co^{2+} and Fe^{3+} ions can either occupy tetrahedral (A) or octahedral (B) sites. The ferrimagnetic behavior of cobalt ferrite can be justified with the coupling between octahedral and tetrahedral sites. Ferrimagnetic behavior is exhibited below 860 K, which stands for the cobalt ferrite Curie temperature. **[20]**
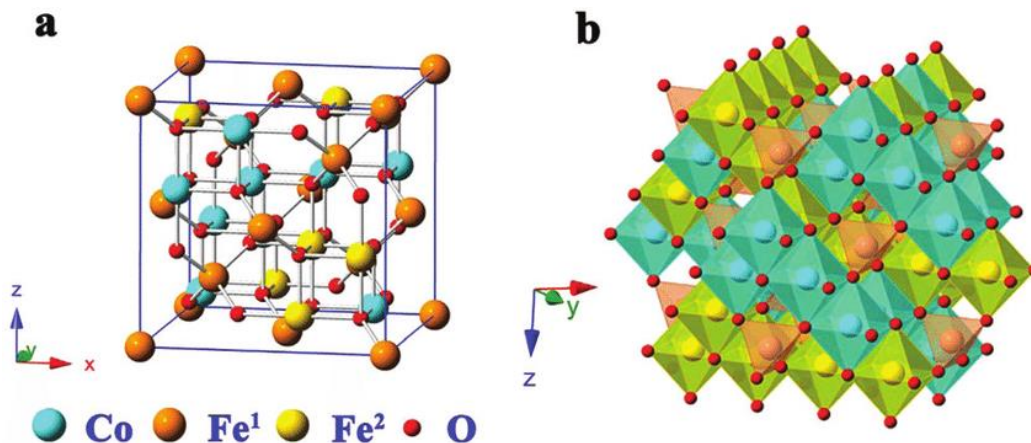
Figure 9. Representation of the CFO structure, [21]

Another important property of CFO, which definitely gives the justification of this research, is high saturation magnetostriction, which has a value of around 200 ppm. **[22]**

As described, due to its excellent properties and versatility, CFO is a justified magnetostrictive component.

Barium titanate

Another compound researched in this work is barium titanate (BaTiO$_3$, BT). Barium titanate is one of the most widely researched ferroelectric material due to its excellent properties such as high Curie temperature and high piezoelectric constants. Its piezoelectric constant, d$_{33}$, is reported to be in the range from 190 pC/N – 260 pC/N. **[23]** Additionally, it is a lead free material, thus an excellent environmental friendly material.

Barium titanate's electrical properties can be greatly enhanced by doping but this is not a concern of this research. Here, the research is focused on its coupling with magnetic particles in order to exhibit magnetoelectric coupling.

BT adopts a perovskite structure having a general formula of ABO$_3$ where Ba^{2+} is A, Ti^{4+} is B. Moreover, Ba^{2+} ions have a coordination number of 12 and Ti^{4+} has a coordination number of 6. **[24]** The schematic representation of the perovskite structure is shown on figure 10.
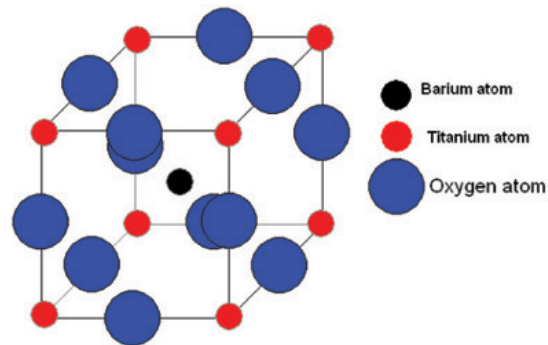
Figure 10. Schematic representation of BT perovskite structure, [25]

Its structure is highly influenced by the temperature (Curie temperature). More precisely, at 130 °C it experiences a phase change from tetragonal to cubic symmetry, where the high temperature phase is cubic. The interest of this research is definitely the tetragonal symmetry that is ferroelectric. The cubic symmetry is paraelectric and non-piezoelectric. When the transformation from cubic to tetragonal phase is occurring, displacement is occurring too. As a consequence of the ion displacement, opposite charged ions will be accumulated on the sides and dipoles will be created. **[26]**

Additionally, it has been proven that the ferroelectric behavior of BT disappears when the particles have a smaller size than 120 nm. [27]
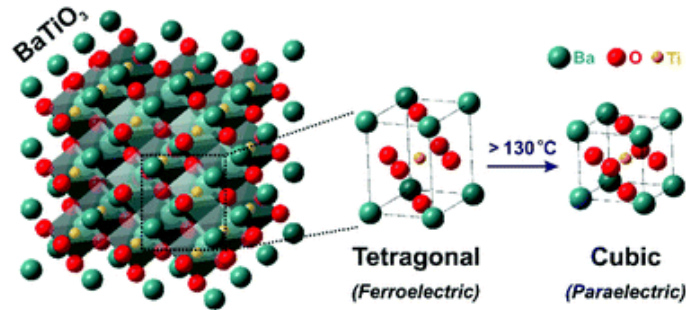
Figure 11. Currie temperature influencing the structure of BT, [28]

Due to the fact that the ABO_3 perovskite structure is pretty flexible and can incorporate a large amount of vacancies, BT is usually doped. Therefore, to enhance its piezoelectric properties, BT is usually doped with elements such as strontium, zirconium and bismuth.

Finally, due to its great ferroelectric properties, BT is a justified selection for a ferroelectric component for the coupling with CFO.

Coupling between CFO and BT – composite nanoparticles

In this part, multiferroic coupling is described. It was proven that composite multiferroic materials exhibit a much larger magnetoelectric effect than single phase materials. Magnetoelectric coupling is generated through the mechanical strain that arises at the interface between the two components. This strain is generated either by the application of the magnetic or electric field. The coupling can be furthermore enhanced when dealing with the nanostructured materials. This can be explained as a higher density of interfaces the lower the size of the particle is. Therefore, in this research the focus is on coupling between the nanoparticles. Furthemore, in this research, a multiferroic phase is constituted by a ferroelectric component that is barium titanate and ferromagnetic component which is cobalt ferrite. Also, due to the spinodal decomposition of these particles at high temperatures, no interactions will occur between them. Furthermore, magnetoelectric coupling at the room temperature is somewhat weak. This kind of coupling can be improved by several orders of magnitude in the form of composite materials, which is definitely the aim of this research.

2.6. Basic principles and protocols of the techniques used for the characterization of the composite nanoparticles

Here, all the protocols of the techniques used to obtain the results in the experimental part are listed. Firstly, all of the techniques were theoretically explained and later on the specific protocol. Techniques used to characterize the nanopowders were: Scanning electron microscopy (SEM), Transmission electron microscopy (TEM), Fourier transform infrared spectroscopy (FTIR), X Ray Powder Diffraction (XRD) and Alternating magnetometer gradient measurements (AMG).Also, toxicity measurements' by CyQUANT Lactate dehydrogenase (LDH) Citotoxicity Assay Kit are explained in the following text.

SEM

Basic principles

Dealing with nanoscale particles, optical microscopes are not able to provide any useful information due to their limits to visible light. In order to characterize the morphology, texture and composition of the nanopowders, it is necessary to apply a beam of accelerated electrons in vacuum. Electrons are characterized by higher energy and lower wavelengths that the light. In SEM, depth of focus is much improved and magnification can be much higher than in the case of the optical microscope. SEM can provide a magnification of up to 150 000x thus being able to give a detailed information of the nanoscale powders. **[30]**

Scanning electron microscopy is a type of electronic microscope that uses a beam of focused high energy electrons in order to obtain an image which gives information about sample's composition and topology (texture). Most of the times, data is collected from a selected area in a form of 2D image. Having said that selected areas can be investigated, it gives an opportunity to perform a semi quantitative or quantitative analysis with EDS obtaining the chemical composition.

By applying an accelerated beam of electrons to a sample, interactions between the sample and electrons occur. As a result of these interactions, secondary electrons, backscattered electrons and characteristic X Rays are formed. These signals are then collected by a detector to construct a SEM image. Basically, the beam of accelerated electrons penetrates the sample in a depth of few microns. Backscattered electrons, as the name says, are backscattered as a result of elastic interactions between the sample and the electrons. Knowing the fact that larger is the atom of the sample, stronger is the scattering, larger atoms will produce a higher signal. Namely, larger is the atomic number of the atom, more backscattered electrons will travel to the detector. This differentiation of the atomic number gives the ability of converting local

difference in chemical composition into image contrast. BSE have also the ability to give information about crystallography and magnetic field. **[31]**
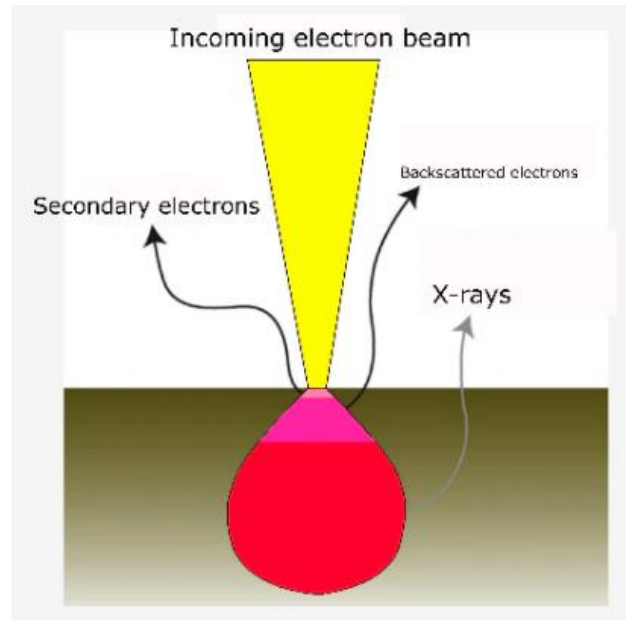
Figure 12. Schematic representation of the interactions among the accelerated electron beam and the sample, [31]
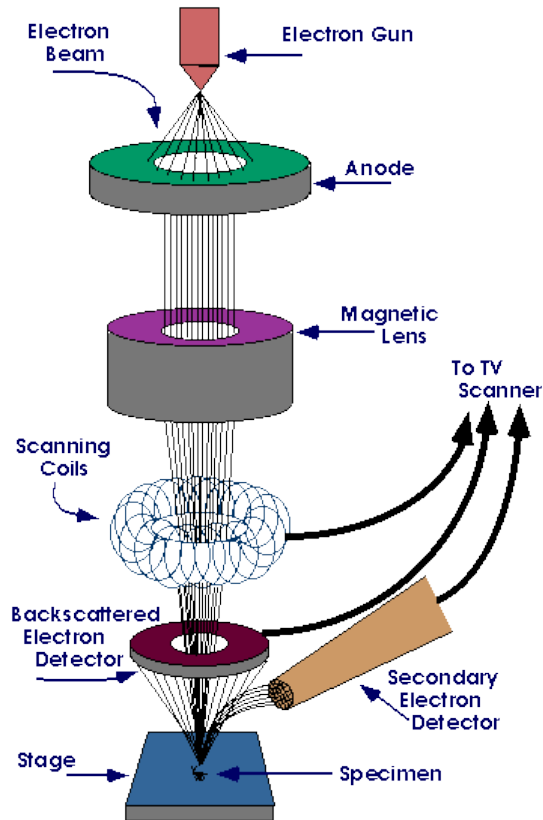
Figure 13. Scheme of SEM, [32]

Mainly used BSE detectors are based on PN junctions where electron-hole pairs are generated by the BSE and later on are separated by the detector. To have the highest possible collection of BSE, detectors are placed on top of the sample. When all the detector parts are enabled, chemical composition can be retrieved. This collection is based on the contrast where heavier elements are brighter on the image. Enabling only specific parts of the detector, topology is retrieved.

To make a clear distinguishing between the backscattered and secondary electrons, it is important to point out their origin. More precisely, secondary electrons originate from the surface or near the surface region. Also, they are obtained by inelastic interactions and they are characterized by a lower energy than the backscattered electrons. To detect them, Everhart-Thornley detectors are most commonly used. These detectors contain positively charged scintillators, which attract the electrons and as a result light is obtained. Everhart – Thornley detectors are placed on the sides of the chamber in order to achieve the highest possible efficiency of collecting the electrons. Secondary electrons give more detailed surface characterization than the backscattered electrons. **[33]**

To obtain an even higher resolutions and a better insight of the internal sample structure, transmission electron microscope is used. However, TEM requires a special training and more knowledge and it is much more expensive.

Protocol:

Scanning electron microscopy (SEM) with the TESCAN VEGA3 was used to characterize the size, morphology, and chemical composition of the NPs. First, the desired test sample was prepared similarly to the DLS samples, i.e., with a concentration of ~0.143 mg/mL. Afterwards, one drop of the test sample was drop-casted onto a SEM sample plate, which was lined with a double-sided adhesive carbon tape. The solvent was allowed to evaporate at room temperature in the fume hood. The SEM sample plates were then sputtered with a 4 nm layer of platinum (ρ = 21.45 g/cm^3) in a vacuumed chamber using the Baltec MED 020 Coating System. Subsequently, the SEM sample plates were placed inside the TESCAN VEGA3 machine and proceeded with SEM microscopy using the TESCAN VEGA software. Images were captured at 10 000x, 40 000x and 95 000x magnification, and saved as PNG images. Energy-dispersive X-ray spectroscopy (EDS) analysis was also completed with the TESCAN VEGA3. The EDS probe was inserted into the device and proceeded with EDS analysis using the Espirit Compact software. EDS images and graphs were saved in PDF format.

As previously denoted, to get a better insight into the complete sample structure, TEM analysis can be performed. In the next chapter, principles of TEM are explained. TEM investigation was done in the collaboration with Facultat für Physik from Karlsruhe Institute of Technology.

TEM

Transmission electronic microscope is another type of electronic microscope that uses beam of electrons to produce an image. This microscope uses a broad beam of electrons in order to get an insight of the internal material structure. More precisely, a beam of electrons is transmitted through the sample in order to get its composition, morphology and structure.

In order to be able to successfully perform TEM analysis, it is mandatory for samples to be thin, thinner than 150 nm. These electrons that pass through the sample are collected by the detector and the image is formed. TEM gives the ability to reach a magnification potential of 10-50 million times, being microscope that gives the highest resolutions amongst all. **[34]**

The basic working principle of TEM can be explained as follows.

The basic TEM is constituted by four working parts: electron beam source, lenses, sample holder and an imaging system. **[35]**
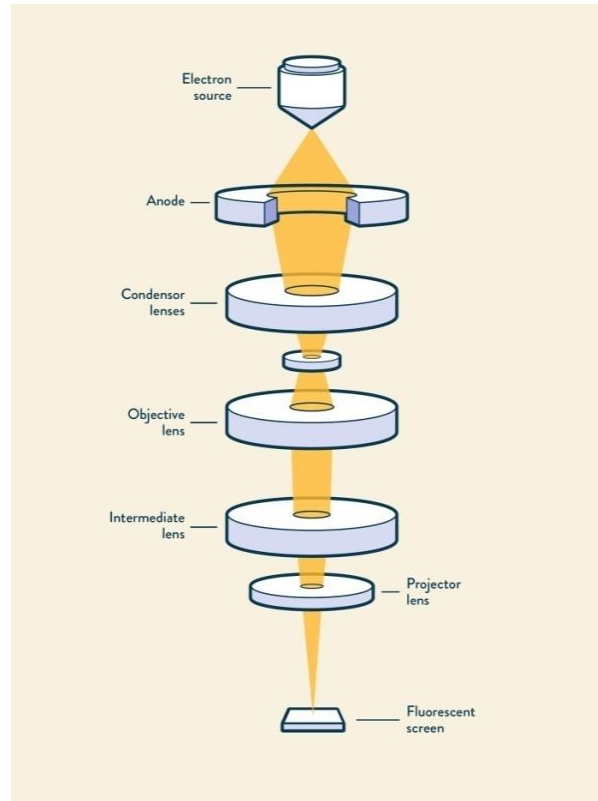
Figure 14. Schematic outline of TEM, [34]

The electron beam source is constituted by two parts – anode and cathode (denoted as an electron source). The most common electron source is made of tungsten that emits electrons when heated up. As denoted on the picture, anode is perforated in order to have a better focus of the emitted electrons. This means that only electrons having high enough energy will be able to pass through the anode thus electrons will have a well defined energy. This aperture is basically working as a filter. (Figure 14) The imaging system consists of intermediate lenses, projector lenses and a fluorescent screen. **[35]** Going from objective lenses to projector lenses, aperture is progressively getting more and higher magnification is achieved. More precisely, intermediate lenses are refocusing the electrons that pass through and projector lenses are used to projectthem to the image. Intermediate lenses provide an image magnification, while projector lenses provide an even better magnification with respect to the intermediate lenses. In the next step fluorescent screen is used to see the image. It is also constituted by a camera that records the image. The formed image is made of black and grey parts, the less the electrons pass through,blacker is the part.

However, TEM can successfully provide chemical composition, distributions and grain size of the sample.

A big advantage of TEM is that it can successfully examine materials having a non-uniform density. Moreover, more electrons pass through the more the material is porous. **[36]**

When being compared to SEM, it is definitely more costly and it requires more knowledge and training to be able to use it. At the same time, it requires longer times and more sample preparation, but it definitely gives more information and better quality images.

XRD

X Ray Diffraction is another powerful technique being able to provide information about material's crystallographic structure. Other than that, it is able to evaluate some other structural parameters, such as preferred crystallographic orientation, average grain size, defects and present strains.

It based on the act of incident X Rays on the material and measurement of scattering angles that X rays leave. In order for material to be eligible for XRD analysis, it needs to have a certain order in its structure, hence crystallinity.

Crystals can be thought as regular arrays of atoms. When the material is irradiated with X rays, X rays will interact with electrons. **[37]** As a result of these elastic interactions, regular spherical waves would be produced. As well known, waves are subjected to interference which can either be constructive or destructive. If destructive interference occurs, these spherical waves will cancel each other. However, XRD is based exclusively on the constructive interference. In the case of the constructive interference, the resultant wave is will be amplified. **[38]** The peaks obtained by XRD are related to the atomic distances.
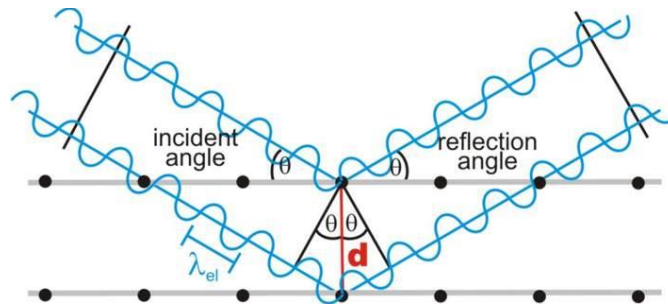
Figure 15. XRD schematic representation, [39]

When taking a deeper look into the crystalline structure, periodic arrays of atoms are thought of planes and a crystal is constituted by many parallel planes being spaced by a certain length d. More precisely, when an X ray strikes the material with a certain angle Ө, it will be further reflected by the same angle Ө. Bragg's law gives an important condition for a constructive interference which is given by the following:

$$n\lambda=2d\sin\Theta$$

Where n is an integer; λ wavelength; d spacing between the planes and Ө an angle.

The Bragg law states that the scattered radiation undergoes a constructive interference only if the differences in the wavepath (i.e. wavefronts) correspond to an integer times wavelength. More precisely OA+OB should be equal to nλ.

By knowing the wavelength of the incident beam, angles at which the beams leave material are measured (Ө). From the Bragg's equation, spacing between the planes can be found.

In this work, powder diffraction has been performed. It is based on orientation from 0 to 90° where all the orientations are recorded. Each of these orientations will correspond to a different atomic spacing. Finally, atomic spacings are converted into angles.

Protocol

XRD was another technique used for identification of the synthesized nanopowders. In this master thesis, Bruker D8 XRD machine was used. To obtain a diffractogram, DiffracEva software was used. And final results are saved in the form of PDF.

Initially, all the powders were carefully applied onto the Si wafer with the orientation (111). Previously, wafers were carefully cleaned with ethanol and later on placed onto the sample holders. As mangetoelectric powders were examined, little magnet was placed underneath the wafer in order for powder to be centered. As previously denoted, Bruker D8 XRD machine was used to perform the measurements. All the samples were parallelly stacked into the column and the XRD chamber was closed. After that, X Rays were turned. In the next step, operating conditions were set. More precisely, all the measurements were performed with a voltage of 40 kV and current of 40 mA. Angle of diffraction was set from 5-45° as it was expected for peaks of BT-CFO to appear in this range of angles. Increment of an angle was set to be 0.015°. Moreover, lower is the increment, longer are the times of measurements but more accurate are the results.

After the measurements were finished, software DiffracEva was used in order to characterize the powders. The final diffractograms were saved in PDF.

FTIR

Fourier transmission infrared spectroscopy is another technique used to confirm the composition and structure of the nanoparticles. It lies on a fact that each functional group when irradiated vibrates at the characteristic wavelength. This technique measures absorbance or transmittance to determine the composition. In this research, obtained spectra are assessed measuring absorbance. **[40]**

FTIR uses a near IR range of frequencies to irradiate a material. Outcome of the radiation is a change of the dipole moment.

When molecule absorbs the light, its vibration is excited. A molecule can vibrate in different ways and each mode is called vibrational mode. The number of vibrational modes characteristic of a molecule can be determined according to the following rule: 3N-5 for linear molecules and 3N-6 for nonlinear molecules where N is the number of atoms. Furthermore, vibrational modes are divided into 2 main groups, which are stretching vibrations and bending vibrations. As shown on the picture, stretching vibrations can be symmetrical or asymmetrical and they change the bond length. On the other hand, bending vibrations alter the bond length and they can be further divided into twisting, rocking, wagging and scissoring. **[41]**
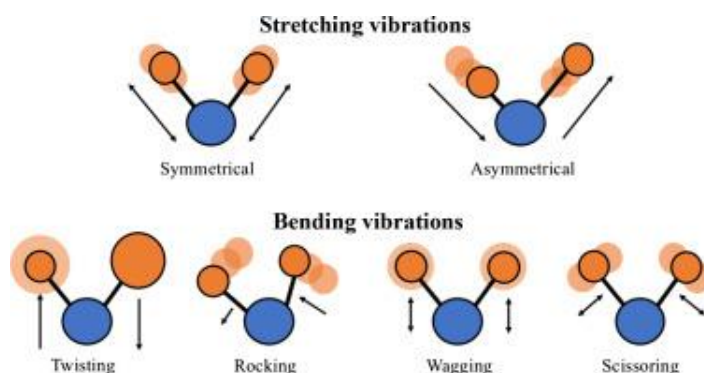

Figure 16. Schematic representation of the molecule vibration modes, [41]

Additionally, to be able to label the peaks on the correct way, it is important to know whether they are strong or weak. In the image below, some specific functional groups, their ranges of frequencies and peak intensities are presented.

IR Absorptions of Common Functional Groups		
Functional Group	*Absorption Location (cm^{-1})*	*Absorption Intensity*
Alkane (C–H)	2,850–2,975	Medium to strong
Alcohol (O–H)	3,400–3,700	Strong, broad
Alkene (C=C)	1,640–1,680	Weak to medium
(C=C–H)	3,020–3,100	Medium
Alkyne		
(C≡C)	2,100–2,250	Medium
(C≡C–H)	3,300	Strong
Nitrile (C≡N)	2,200–2,250	Medium
Aromatics	1,650–2,000	Weak
Amines (N–H)	3,300–3,350	Medium
Carbonyls (C=O)		Strong
Aldehyde (CHO)	1,720–1,740	
Ketone (RCOR)	1,715	
Ester (RCOOR)	1,735–1,750	
Acid (RCOOH)	1,700–1,725	

Figure 17. Typical functional groups and their frequency ranges, [42]

However, in this work, FTIR based on the attenuated total reflection (ATR) is used and the working principle of this kind of FTIR will be explained. ATR accessory is composed by reference material (usually diamond) that has a higher refractive index than the sample. **[40]** As known, total internal reflection occurs in the material characterized by a higher refractive index, hence optically denser media. However, in order to have a successful TIR, an essential condition needs to be satisfied where an angle of an incident beam Ɵ$_1$ needs to be equal or higher than a critical angle Ɵc. Mathematical representation of the total reflectance is given by the Snell's law:

$$n1 sin\theta1 = n2 sin\theta2$$

Where n is a refractive index and n1 > n2.
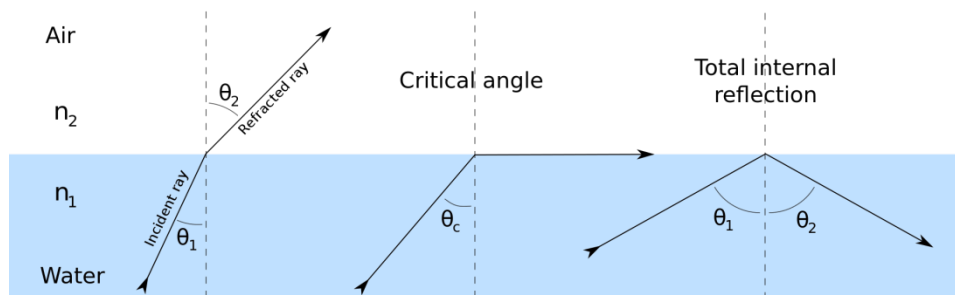

Figure 18. Graphical representation of the total internal reflection, where n1 is optically denser media, [43]

Electromagnetic waves are composed of electric and magnetic component. When total internal reflection occurs, to satisfy continuity, one part of the electric component is transmitted into the area having lower refractive index and this wave is called evanescent wave. This wave

decays exponentially but it cannot be neglected. ATR is based on measuring the evanescent wave. (Figure 19)
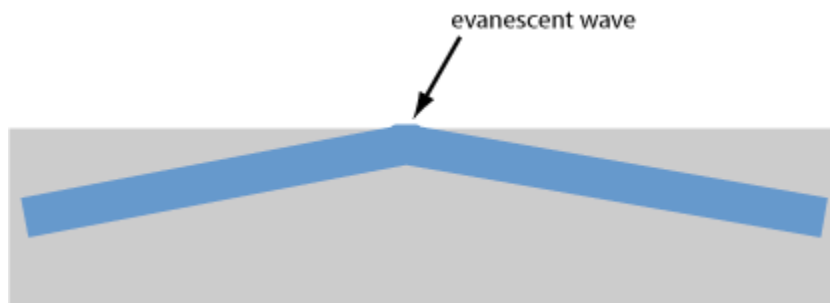
Figure 19. Schematic representation of the evanescent wave, [44]

Protocol

For characterization of BT-CFO nanoparticles, Bruker Tensor Hyperion was used. The software used to obtain the final results was Opus.

Main advantage of this technique is that both liquid and solid samples can be investigated and the use of the machine is rather simple. Before proceeding with measurements, it was important to make sure that surfaces are clean. Cleaning was done by a solution of ethanol and water where ethanol was in 70% mass. In the next stage, operating parameters were set. The window of frequencies of the incident light was from 350 cm^{-1} to 4500 cm^{-1}. Then background had to be set which in this case was diamond. After the background was scanned, the sample was placed in the sample holder. Before proceeding with measurements, it was important to check if the attenuation occurred when the rays were applied. When the successful attenuation is reached, samples can be scanned. As previously denoted, the final results were obtained using the OPUS software after which data was saved in the form of data point table (dpt). For the final representation of the obtained spectra, a program Spectragryph was utilized.

Figure 20. Bruker Tensor Hyperion, Institute of Functional Interfaces, Karlsruhe Institute of Technology

AGM

The alternated gradient magnetometer (AGM) applies an alternating magnetic force onto the sample. In this work, Micromag Model 2900 (figure 21) was used to perform the measurements. Its operation is based on the application of gradient field onto the sample that is vertically hanged in DC field. The sample is vertically mounted on the extension rod (figure 22) that is connected with a piezoelectric element. Alternating field produces an alternating force on the sample which will cause a deflection of the sample. Finally, the deflection is transmitted to the piezoelectric sensing element.

Figure 21. Migromag 2900 AGM, Karlsruhe Institute of Technology, Institute for Functional Interfaces, Karlsruhe Institute of Technology

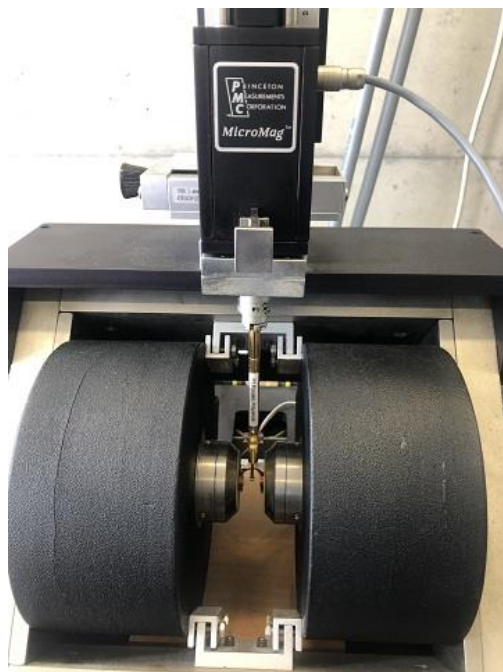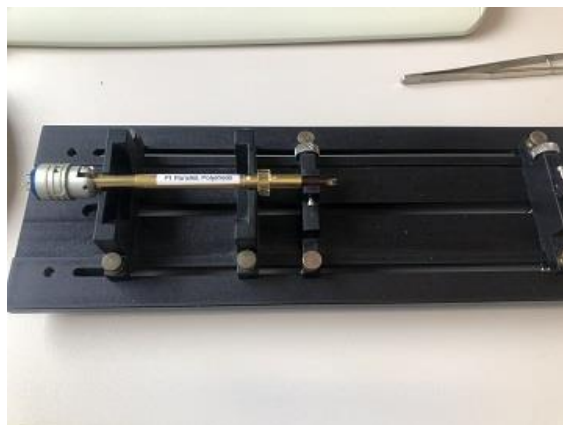**Figure 22. Extension rod, Karlsruhe Institute of Technology, Institute for Functional Interfaces, Karlsruhe Institute of Technology**

Protocol

Initially, sample preparation was performed. Samples in the quantity range from 1-5 mg were put onto the tape. The tape was sealed so no air was entrapped and finally mass of the sample was measured.

The next step is to perform a calibration of the nickel plate, which will be utilized as a reference. To do so, glue was placed onto the sample holder and then nickel plate was stacked. The plate was adjusted carefully and autotune was performed. In the next step, measurement is performed where direct moment versus field was recorded and hysteresis loop was obtained. Finally, normalization by the mass was necessary and data was saved in the form of PDF. In analogy with the reference plate, all the measurements were performed and magnetic loops obtained.

Toxicity measurements

Toxicity investigation of the synthesized nanoparticles has been done by CyQUANT Lactate dehydrogenase (LDH) Cytotoxicity Assay Kit. This kit provides reagents that are able to quantify the cellular cytotoxicity based on the color change. The assay is done by taking an aliquot to the plate and the reaction mixture is added in the next step. After half an hour of the room temperature incubation, the reaction is stopped by the stop solution and in the next step absorbance was measured. As a toxicity indicator, LDH concentration in media was used. Moreover, when the plasma of the cell is damaged, cell membrane releases LDH to the outer media. LDH from the outer media is quantified by a coupled enzymatic reaction where LDH acts as a catalyst promoting the conversion of lactate to peruviate via NAD+ reduction to NADH. The finally obtained oxidation product called red formazan is measured spectrophotometrically at 490 nm. The amount of the red formazan is directly proportional to the amount of the released LDH to the outer media of the cell, hence cytotoxicity. **[45]**

Protocol

To get a better grip on the used chemicals in these measurements, the list of them is represented in the table:

Table 1. Representation of the required items for the cytotoxicity measurements, [45]

Item	Storage
Substrate mix	
Assay buffer	
Lysis buffer	All -20 $^\circ$C protected from light
Stop solution	
LDH positive control	

However, not all the items are included in the Kit. The extra needed items are listed below:

- Cultured cell line
- Tissue culture 96-well plate

- Flat bottom, clear, 96 well plate
- 1% bovine serum albumin (BSA) in phosphored buffered saline (PBS)
- Spectrophotometer microplate reader

Before starting the measurements, it is necessary to prepare the reaction mixture, which is done by mixing the buffer stock solution and substrate stock solution. The mixture should be protected from the light until its use. In the next step, LDH positive control is prepared. Moreover, it is diluted with the buffer stock solution in phosphore buffered saline.

Additionally, it is important to determine the optimum number of the cells. This is done by preparing two series of solution triplicates. First series is used to determine the maximum LDH release in the outer environment. The later is used to determine the spontaneous release of LDH. After that, cells are incubated overnight at 37 °C with an adequate quantity of CO_2. To the set representing the maximum release of LDH, Lysis buffer is added and the mixture gently mixed. In the next step, clear cell plate was also incubated at 37 °C with an adequate quantity of CO_2 and then each sample medium to a 96 well flat-bottom plate in triplicate wells. Finally, an aliquot of reaction mixture was added to the sample well and again incubated at the room temperature. [45] After the addition of the stop solution, absorbance was measured and cytotoxicity measured by the following formula:

$$\% \ cytotoxicity = \frac{\text{compound treated LDH activity} - \text{spontaneuous LDH activity}}{\text{maximum LDH activity} - \text{spontaneuous LDH activity}} * 100$$

In the experimental part in the toxicity measurements section, obtained results are reported and explained. There, results are given in the form of viability. Viability is a measurement of toxicity where 100% of viability stands for null toxicity and 0% viability stands for the highest toxicity.

3. Experimental part

3.1 Synthesis

In this section, the complete sol gel synthesis of mangetoelectric particles will be described. In the following text, the complete procedure of fabrication of magnetoelectric nanoparticles will be described. As previously denoted, there are many different techniques that enable the synthesis of these materials. However, in this research, the chosen method is sol gel due to its low cost and somewhat easy management.

Sol gel process is a wet chemical process that involves two main reactions, which are respectively: 1) hydrolysis of precursor where sol is formed and 2) polycondensation by which gel is obtained. The initially proposed molar ratio between cobalt ferrite and barium titanate was 1:1.4. Also, the synthesis where the molar ratio was 1:1 was performed.

As a starting material, commercial cobalt ferrite nanoparticles are used (Sigma Aldrich 30 nm). They were dispersed in water and the solution was heated up to 80 $^{\circ}$C. As a surfactant, oleic acid was added in 30 % mass with respect to cobalt ferrite. Oleic acid is modifying the surface of the nanoparticles making them hydrophobic. More precisely, oleic acid is constituted by a double bond that has higher ability to lower the surface tension of aqueous solutions being at the same time biodegradable. [46] The obtained solution was heated up to 90 $^{\circ}$C and mixed for half an hour. In the next step, temperature was lowered to 60 $^{\circ}$C and octane was added to the solution. As octane was added, it was immediately possible to see the separation of the two phases by the thin layer of oleic acid. In this step, nanoparticles were transferred from water to octane. The obtained organic phase is called ferrofluid, which is immiscible with the water phase.

In the next step, barium titanate was synthesized. As precursors, barium acetate and titanium butoxide were used. Both of the precursors were dissolved in acetic acid. In order to promote the coupling of cobalt ferrite and barium titanate nanoparticles, stearic acid was used. By mixing the precursors at 90 $^{\circ}$C, white sol was formed and ferrofluid was added. To promote the polycondensation reaction, hence gellation, the effect of two different gelling agents was investigated. Initially, synthesis has been done with 2-methoxy ethanol as a gelling agent. [47] However, no significant loss of viscosity has been observed and the final powders have been obtained by the solvent evaporation. Later on they were calcined at 800 $^{\circ}$C and characterized.

As it is known that citric acid is widely used as a gelling agent, it was used as an alternative gelling agent. More precisely, citric acid monohydrate was dissolved in acetic acid and it was drop wisely added into the solution of barium titanate and cobalt ferrite. It was immediately noticed a high drop of viscosity as carboxylic groups coming from the acetic acid acted as bridges forming a network. As a result, gel was formed.
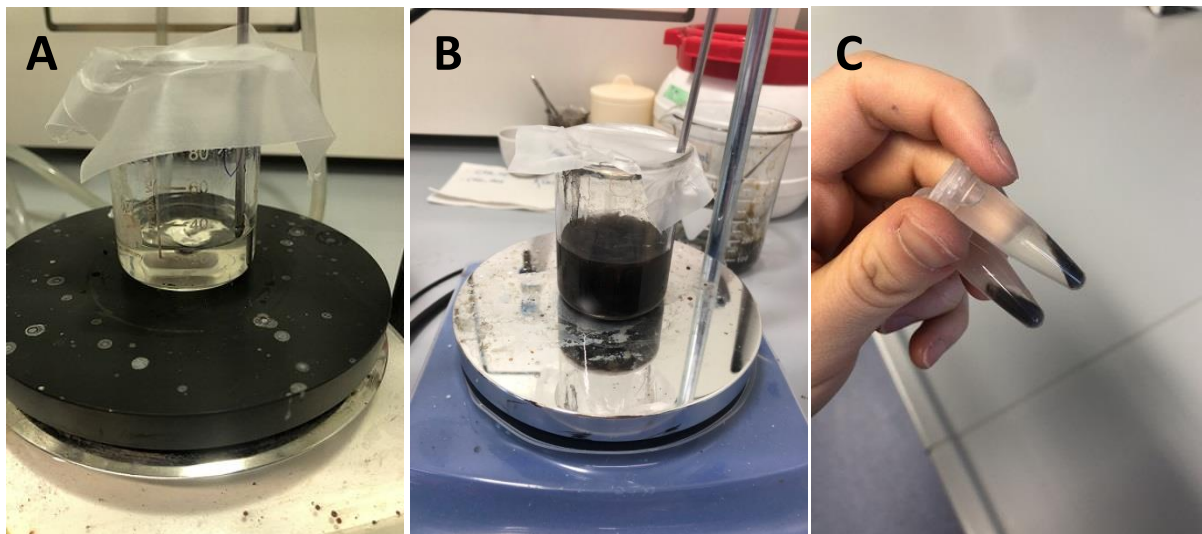
Figure 23. A) bariumtitanate sol; b) addition of the ferrofluid to the sol; c) obtained gels

In the next step, gels were separated from the aqueous phase and then washed three times. For separation and washing step, each centrifuging cycle was performed at 7000 rpm for 5 minutes. After that, gels were dried overnight at 90 °C and calcined at 800 °C at different times. The effect of different times of calcinationwill be discussed in the result section.

The schematic representation of the sol gel synthesis with the citric acid as a gelling agent is given below (Figure 24).In the case when 2-methoxy ethanol was utilized, is that all the solvents were evaporated and the obtained powers were dried and sintered.
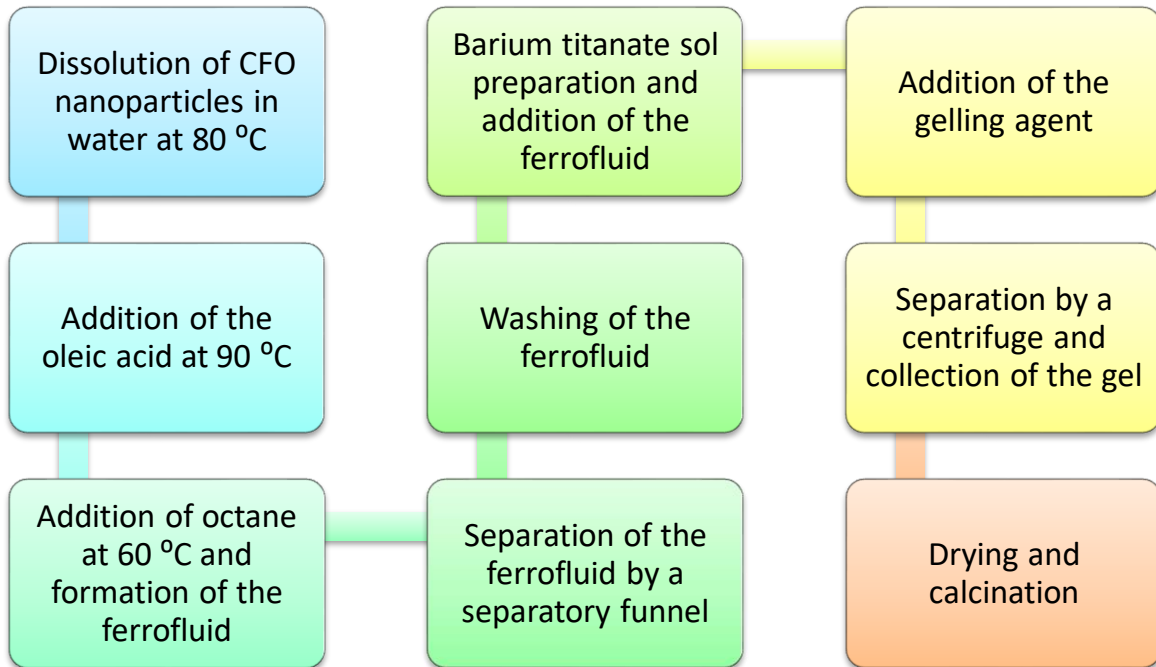
Figure 24. Schematic representation of the sol gel synthesis with citric acid as a gelling agent

4. Results and discussion

This part is dedicated to a detailed characterization of the obtained powders. To determine the morphology and structure of the obtained powders, SEM and XRD were used. To get a better overview of the particles' composition, TEM analysis was performed. The composition was again confirmed by FTIR and EDS. As the aim of this thesis was to produce magnetostrictive particles, it was necessary to perform magnetic measurements. To obtain the magnetic data, VSM was used.

4.1 Scanning Electronic Microscope (SEM) results

SEM was performed in order to get an overview about the morphology of the obtained powders. Moreover, the influence of the mixing time of the ferrofluid at 60 ^{o}C was investigated. In the first case, mixing was performed for 30 minutes only, while in the later, it was performed for 16 hours.

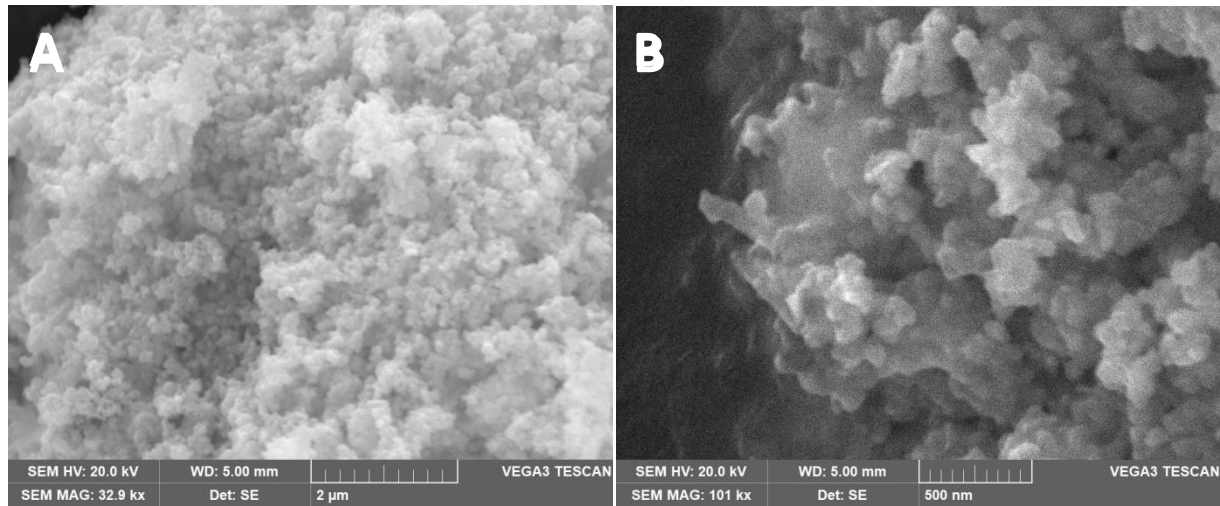*Influence of the ferrofluid mixing times and longevity of reaction steps*

Figure 25. Obtained SEM images from the samples obtained with prolonged reaction timeswhen resolution was a) 2 microns b) 500 nm
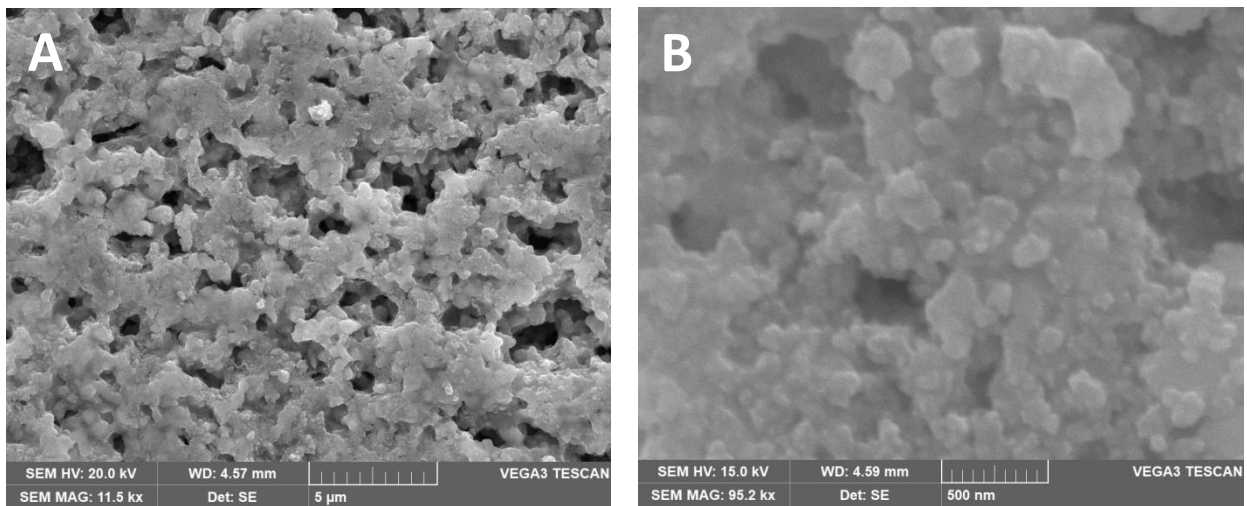
Figure 26. Obtained SEM images from the samples obtained with shorter reaction times when resolution was a) 5 microns b) 500 nm

Observing the SEM pictures obtained for the sample having a longer time of each reactions step (Figure 25), it can be noticed that the particles have a more regular spherical shape that for the samples having shorter time of reaction. It can be also observed that particles were agglomerated in the both cases. This issue can be somewhat solved by the use of a mortar and pestle. Another reason behind the elongation of the reaction times is specifically in the case of ferrofluid formation where much lower losses occurred than in the case when the formation of ferrofluid was performed for 30 minutes only. If the time was increased, CFO particles will have

more time to be transferred to the organic phase, which in this case was octane. Also, prolonging the time of sol formation was beneficial. When the mixing time was just performed for half an hour, particles were less in contact and the porosity was higher. If the particles are not well interconnected, mangetostrictive coupling will be low. It is definitely desirable to have as higher as possible number of interfaces. Therefore, from now on, all the synthesis were performed with longer times of ferrofluid mixing and sol reactions. Also, when the time of sintering was 30 minutes only (Figure 26), higher porosity was obtained than in the case of 1 hour long calcinations.

To get a better grip on the influence of the citric acid as a gelling agent onto the morphology, SEM analysis was performed again. However, SEM cannot give a detailed information about the actual morphology, but it can definitely give an overview about it.
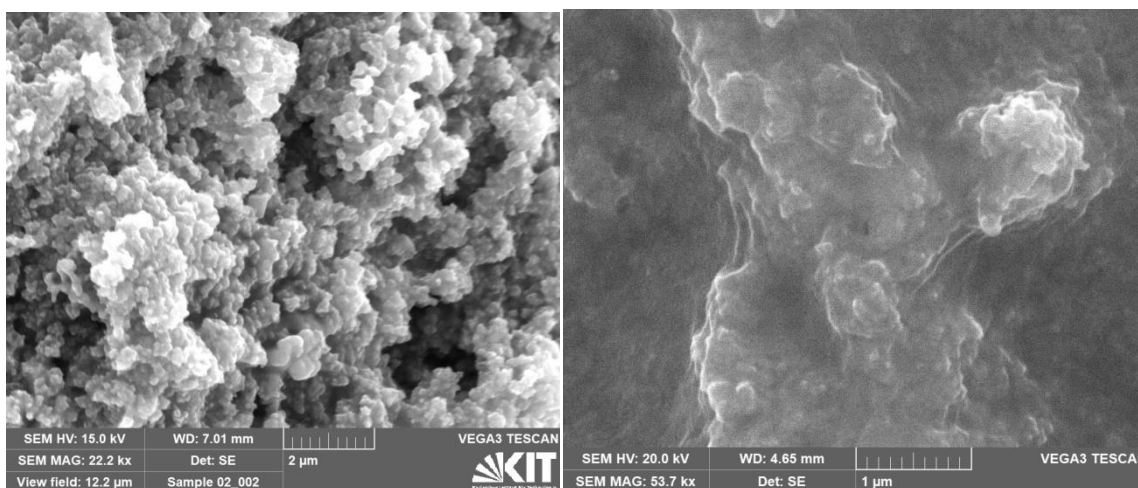
Figure 27. SEM images of the powders obtained with citric acid as a gelling agent

From the SEM images above, it can be noticed that interconnections between the particles were improved when gellation was obtained with citric acid. At the same time, particles can be characterized as agglomerated and of irregular shape. Agglomeration can be somewhat solved, as previously noted, by a mortar and pestle.

At the same time, it was possible to perform an elemental analysis. Although elemental analysis cannot give information about the chemical bonds and formed compounds, it is still giving an overview of the chemical composition.
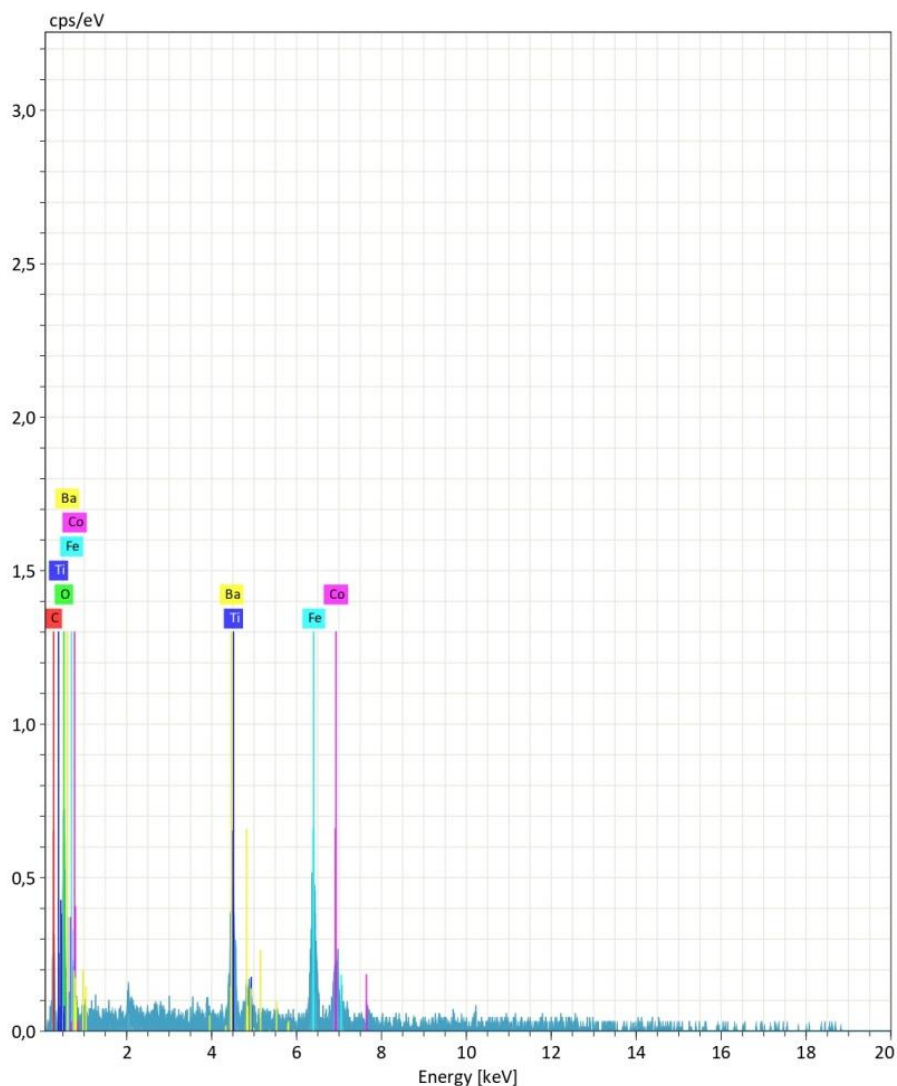
Figure 28. EDS spectra obtained from a sample where 2-methoxy ethanol was used and times of reactions were shorter

From the image above (Figure 28), it can be confirmed that Ba, Co, Fe, O and Ti are copresent. Later on, it will be confirmed that they indeed form $BaTiO_3$ and $CoFe_2O_4$ compounds. At the same time, carbon is present which is an undesirable element and it can be considered as an impurity and its residue can be due to the used organic solvents.

Elemental analysis has been also performed for the sample where ferrofluid has been mixed overnight and citric acid was used as a gelling agent.

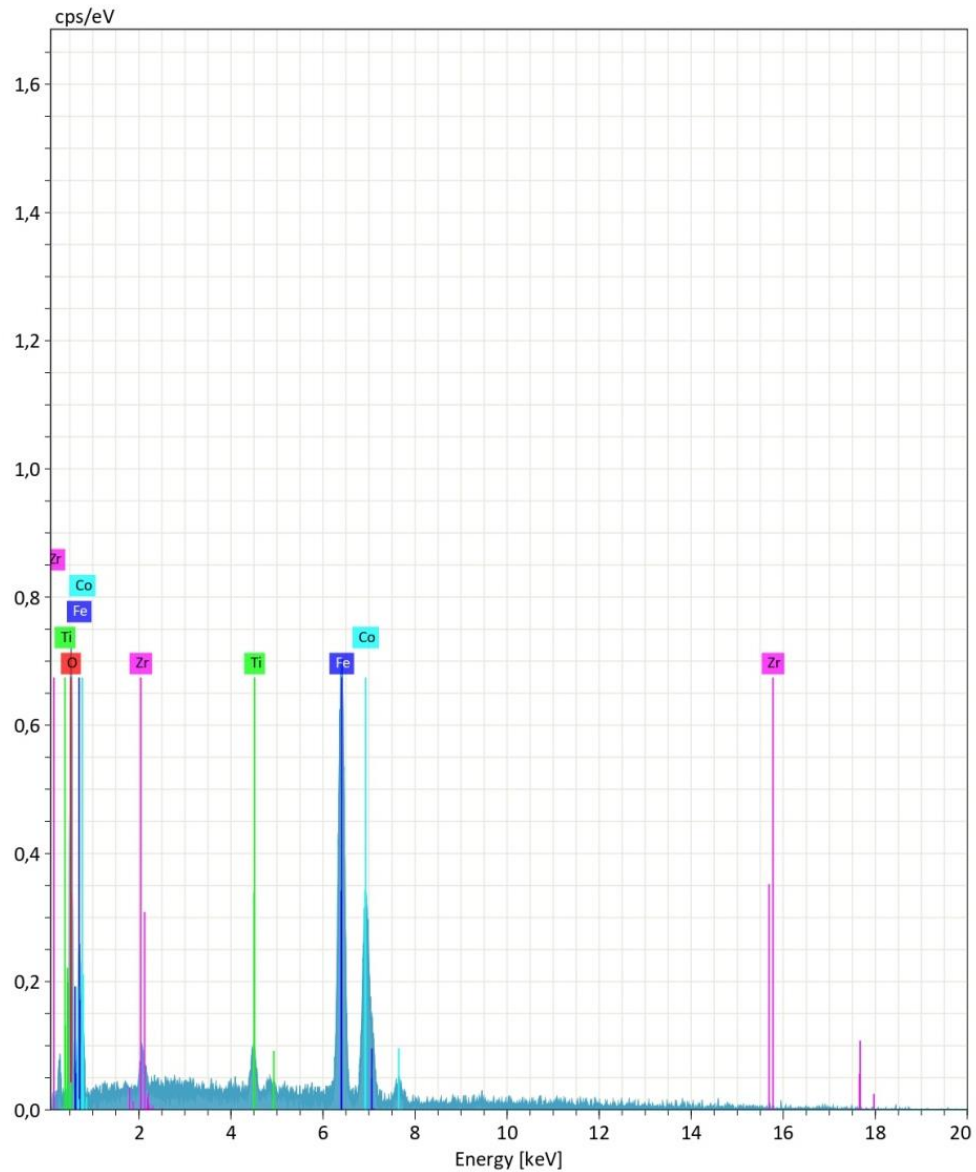**Figure 29. EDS spectra obtained from a sample where citric acid was used as a gelling agent and times of reactions were prolonged**
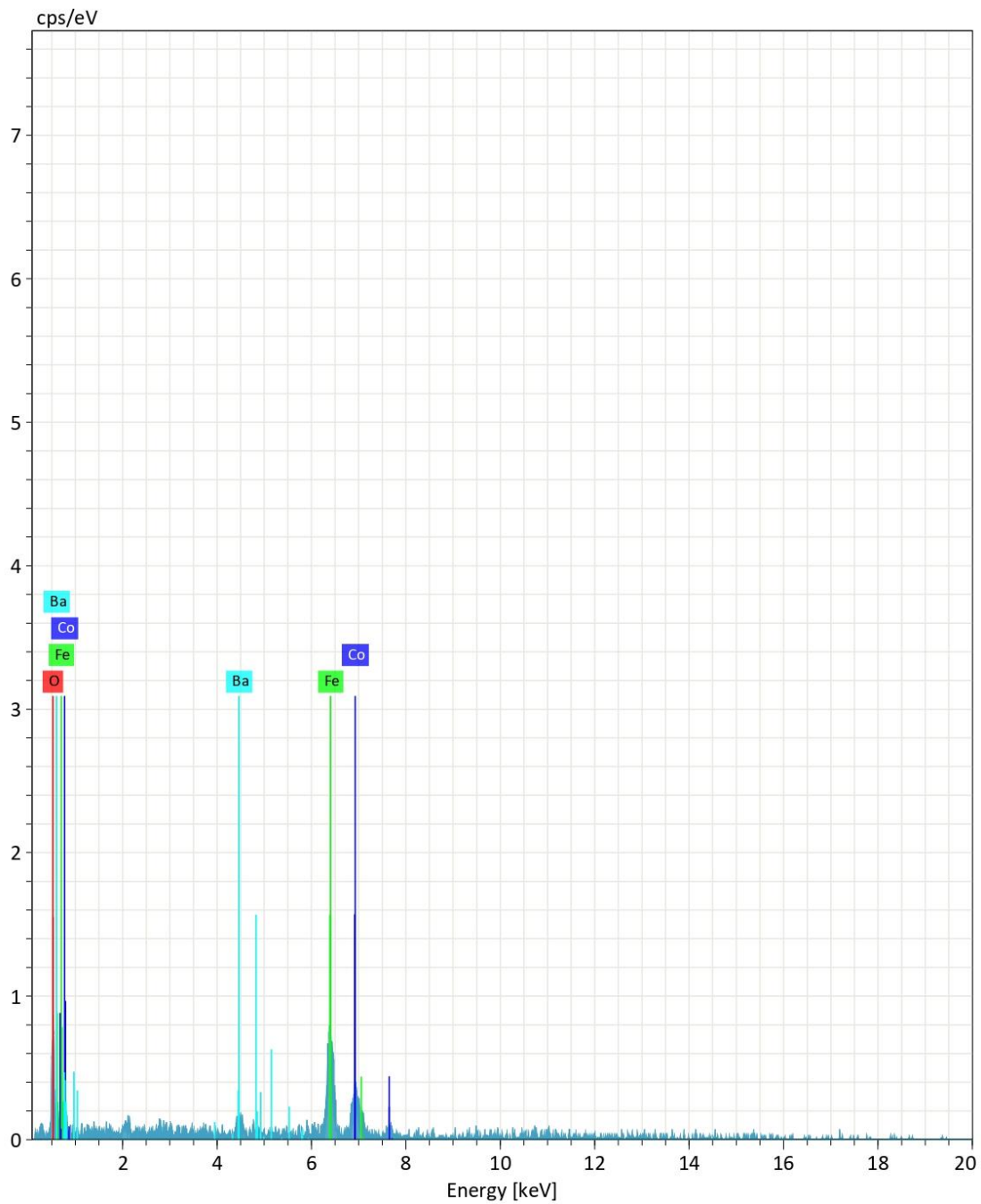
Figure 30. Another EDS spectra obtained from a sample where citric acid was used as a gelling agent and times of reactions were prolonged

By observing the above spectra (Figure 29 and Figure 30), it is confirmed the presence of the desired elements. However, it can be seen that Zr is also present which is definitely undesirable. Since no source of zirconium has been used in the synthesis, it can be concluded that it comes from the equipment, which could have been improperly cleaned before the analysis.

As previously seen, elemental analysis could give an overview about the powders' composition. To know more about chemical bonds between these elements, in the next step, transmission electronic microscope has been used.

4.2 Transmission electronic microscope (TEM) results

HAADF-STEM combined with EDXS was used to investigate the chemical composition of $FeCoO_x$-$BaTiO_y$NPs. The experiments are performed on an FEI Osiris ChemiSTEM microscope at 200 keV electron energy, which is equipped with a Super-X EDXS system comprising four silicon drift detectors. EDXS spectra are quantified with the FEI software package "TEM imaging and analysis" (TIA) version 4.7 SP3. Using TIA, element concentrations were calculated on the basis of a refined Kramers' law model, which includes corrections for detector absorption and background subtraction. For this purpose, standard-less quantification, i.e. by means of theoretical sensitivity factors, without thickness correctionwasapplied. EDXS spectra obtained during scanning of a rectangular area including inside a $FeCoO_x$-$BaTiO_y$ nanoparticle ensemble are used to determine their average chemical composition.

Besides EDXS lines of the corresponding elements, i.e. lines of the Fe-K, Co-K, Ba-L and Ti-K series, as well as, the O-K_α line, X-ray lines of Cu-K and Cu-L series from the grid, the C-K_α line from the amorphous carbon substrate and the Si-K series from substrate contamination are also observed in all EDXS spectra.

Alternatively, EDXS elemental maps of Fe (Fe-K_α), Co (Co-K_α), Ba (Ba-L_α), Ti (Ti-K_α) and O (O-K_α) are recorded and used to investigate their distribution within $FeCoO_x$-$BaTiO_y$ nanoparticles. The maps are analyzed by using the ESPRIT software (version 1.9) from Bruker.

Chemical composition of the nanoparticles by HAADF-EDXS

On the HAADF STEM image, a green frame can be observed that confirms the assemble of $BaTiO_3$-$CoFe_2O_4$ nanoparticles with the resolution of 150 nm. These results were obtained when citric acid was used as a gelling agent and time of sintering was 1 hour.
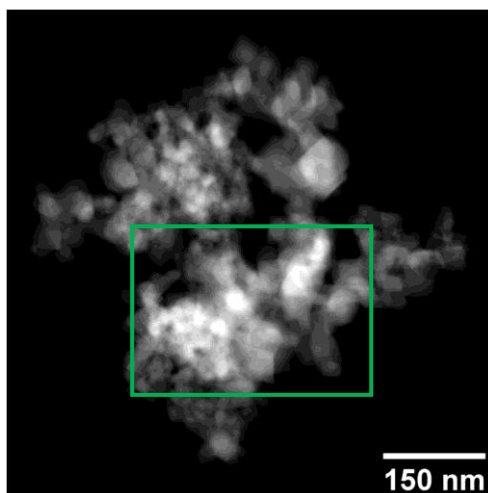
Figure 31. HAADF STEM image

Quantificationofthe EDXS areascanwithinthegreenframe

The chemical composition of $FeCoO_x$-$BaTiO_y$ nanoparticles was further investigated by the quantification of the EDXS spectrum obtained during scanning a rectangular area including inside the ensemble of $FeCoO_x$-$BaTiO_y$ nanoparticles within the green frame in the HAADF STEM image. The quantification results in the average chemical composition of **$Co_{13.9\pm1.0}Fe_{27.9\pm1.0}Ba_{2.0\pm0.2}Ti_{1.8\pm0.2}O_{54.4\pm2.0}$** demonstrating, within error bars, the formation of **$Co_{13.9}Fe_{27.9}O_{48.4}$ - $Ba_{2.0}Ti_{1.8}O_6 \approx CoFe_2O_{3.5}$ – $BaTiO_3$** nanoparticles.
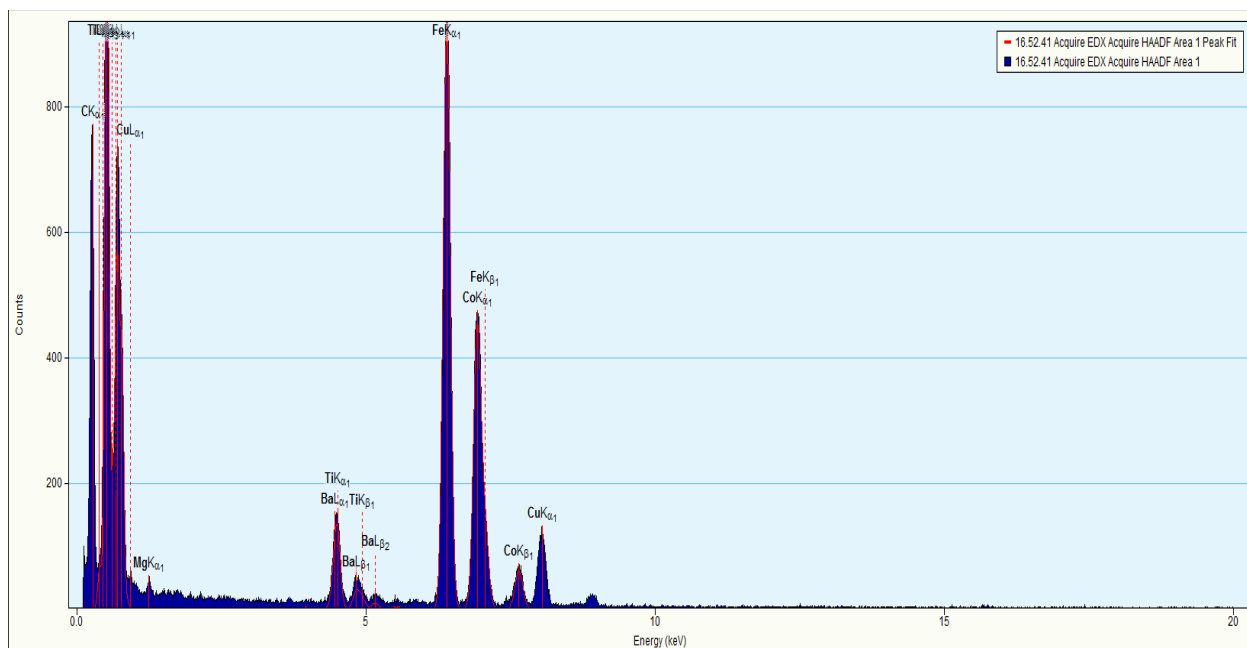
Figure 32. Quantification of the EDXS area scan within the green frame

EDXS elemental maps are used to further investigate the distribution of Fe, Co, Ba, Ti and O within FeCoOx-BaTiOy nanoparticles.

Figure 33. HAADF-STEM image and EDXS maps of Fe (Fe-K$_\alpha$ line - red), Co (Co-K$_\alpha$ line - green), Ba (Ba-K$_\alpha$ line - blue), Ti (Ti-K$_\alpha$ line - orange) and O (O-K$_\alpha$ line - lavender) distributions

EDXS map of O together with the EDXS maps of Fe-Co and Bi-Ti demonstrate the formation of homogeneous $FeCoO_x$ and $BaTiO_3$ nanoparticles, while the EDXS elemental map of Fe-Ba shows that no $FeCoO_x$-$BaTiO_3$ core-shell particles are formed. Instead, $BaTiO_3$ particles are located at $CoFeO_x$ particle boundaries which is accepted as a valid result since the coupling at the interfaces is achieved.
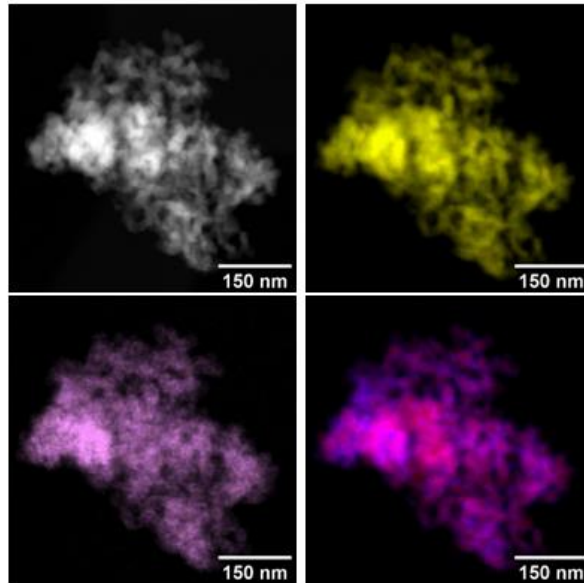
Figure 34. EDX maps O, Fe-Co, Ba-Ti distributions respectively

Chemical compositionofnanoparticlesby HAADF-STEM / EDXS

Again, the HAADF STEM image indicates the formation of large particle agglomerates. Performing a scan within the green frame,it is confirmed that $BaTiO_3 - CoFe_2O_4$ nanoparticles are obtained.
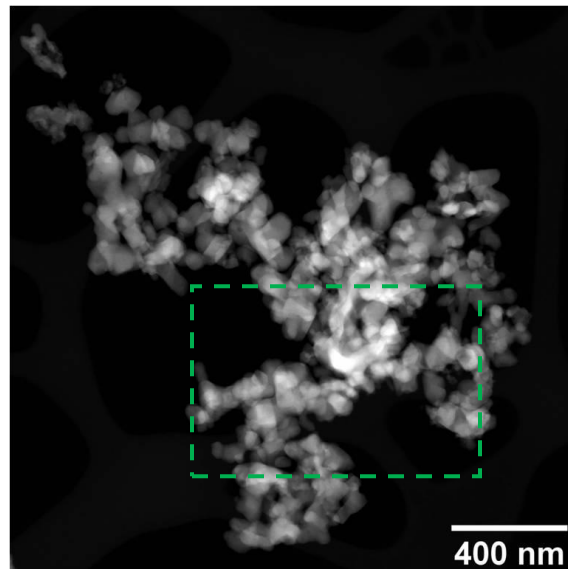
Figure 35. HAADF STEM image

In this case, citric acid was again used as a gelling agent and the time of sintering was higher. More precisely, it was done for 2 hours at 800 ^{o}C.

Quantificationofthe EDXS areascanwithinthegreenframe

The chemical composition of $FeCoO_x$-$BaTiO_y$ nanoparticles was further investigated by the quantification of the EDXS spectrum obtained during scanning a rectangular area including inside the ensemble of $FeCoO_x$-$BaTiO_y$ nanoparticles within the green frame in the HAADF STEM image. The quantification results in the average chemical composition of $Co_{14.1\pm0.5}Fe_{27.5\pm0.5}Ba_{0.2\pm0.1}Ti_{0.2\pm0.1}O_{58.0\pm2.0}$demonstrating, within error bars, the formation of $Co_{14.1}Fe_{27.5}O_{57.4} - Ba_{0.2}Ti_{0.2}O_{0.6} \approx CoFe_2O_4 - BaTiO_3$ nanoparticles.
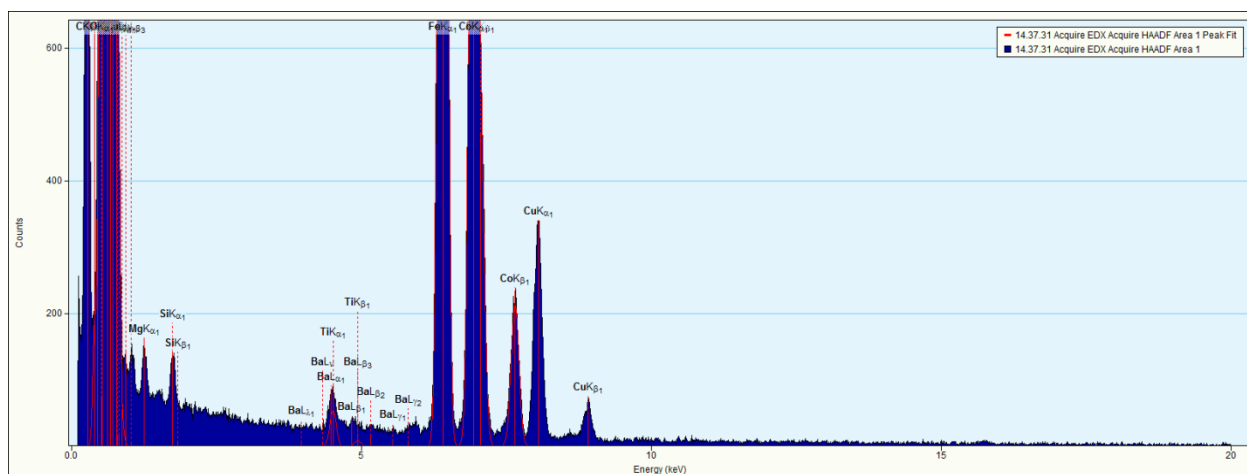
Figure 36. Quantification of the EDXS area scan within the green frame

EDXS elemental maps are used to further investigate the distribution of Fe, Co, Ba, Ti and O within $FeCoO_x$-$BaTiO_y$ *nanoparticle assembly.*
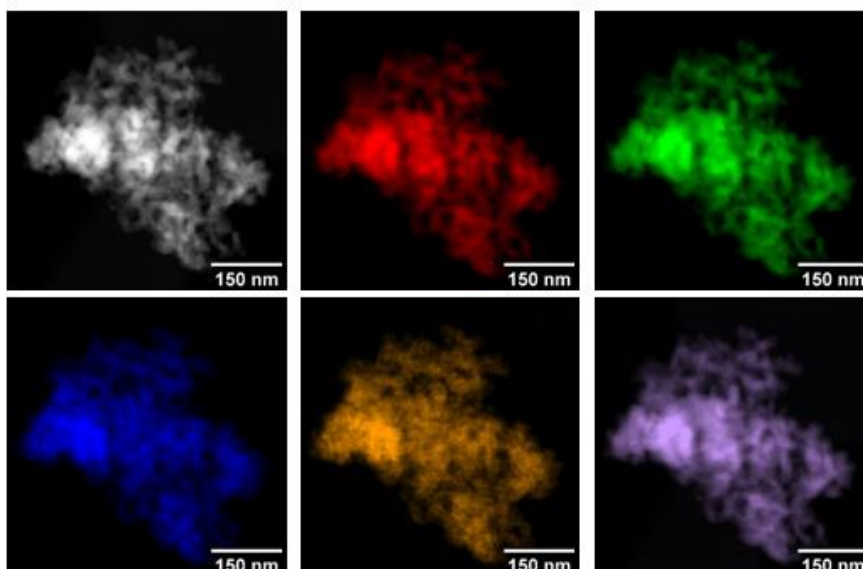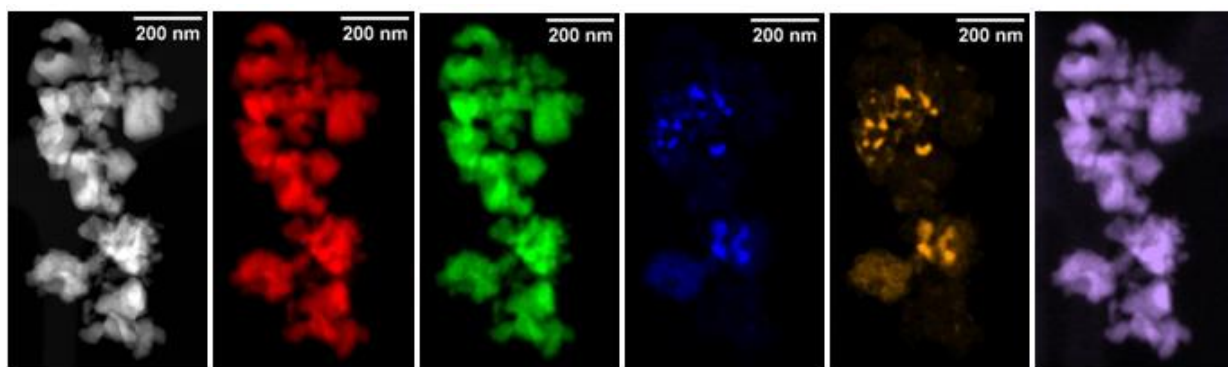

Figure 37. HAADF-STEM image and EDXS maps of Fe (Fe-K$_\alpha$ line - red), Co (Co-K$_\alpha$ line - green), Ba (Ba-K$_\alpha$ line - blue), Ti (Ti-K$_\alpha$ line - orange) and O (O-K$_\alpha$ line - lavender) distributions

EDXS map of O together with EDXS maps of Fe-Co and Ba-Ti confirms the formation of $FeCoO_x$ and $BaTiO_y$ nanoparticles, while the EDXS elemental map of Fe-Ba shows thatBaTiO$_3$ particles are located at boundaries of $CoFeO_x$ particles, hence magnetoelectric coupling has been achieved.
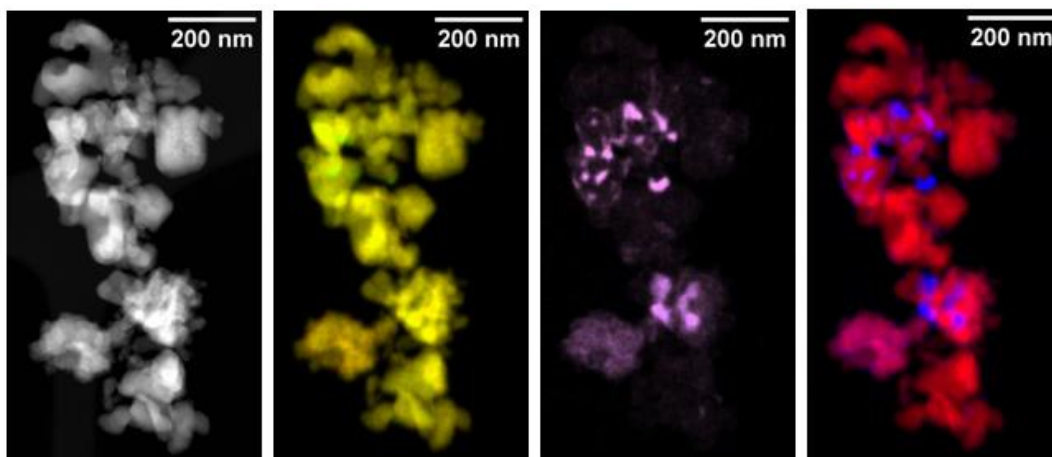
Figure 38.HAADF-STEM image and EDXS maps of Fe – Co, Ba – Ti and Fe – Ba distributions respectively

The next idea of the research was to use a different molar ratio of Barium titanate and CFO. The chosen ratio was 1:1 and powders were sintered for 1 hour at 800 $^\circ$C. The reported TEM results are as follows.

Chemical compositionofnanoparticlesby HAADF-STEM / EDXS
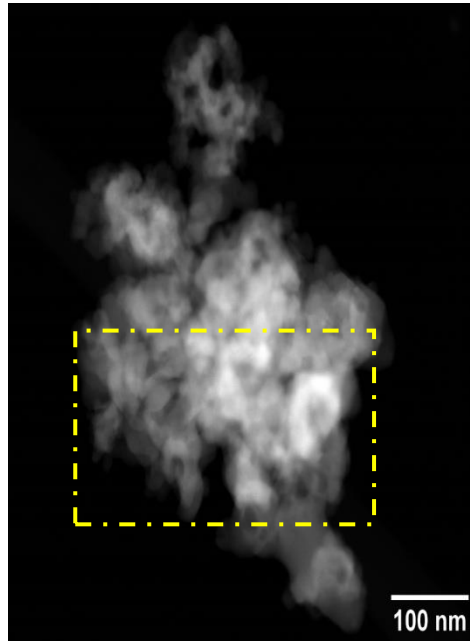
Figure 39. Chemical composition of the nanoparticles

Performing a scan (yellow frame) on the obtain nanoparticles, it was proven that $FeCoO_x$-$BaTiO_y$ nanoparticle ensemble was obtained. At the same time, an agglomeration can be noticed which is a common problem of the sol gel synthesis. This problem can be somewhat solved by milling the particles.

Quantificationofthe EDXS areascanwithintheyellowframe

The chemical composition of $FeCoO_x$-$BaTiO_y$ nanoparticles was further investigated by the quantification of the EDXS spectrum obtained during scanning a rectangular area including inside the ensemble of $FeCoO_x$-$BaTiO_y$ nanoparticles within the yellow frame in the HAADF STEM image. The quantification results in the average chemical composition of $Co_{15.8\pm1.0}Fe_{28.7\pm1.0}Ba_{3.3\pm0.4}Ti_{2.2\pm0.2}O_{50.0\pm1.6}$demonstrating, within error bars, the formation of $Co_{15.8}Fe_{28.7}O_{43.4} - Ba_{3.3}Ti_{2.2}O_{6.6} \approx CoFe_2O_3 - BaTiO_3$ nanoparticles. Due to the fact that with this specific molar ratio, CoFe2O4 nanoparticles were not formed, the future investigation was performed using an initially established molar ratio. However, the complete TEM measurement was performed also in the case of 1:1 molar ratio.
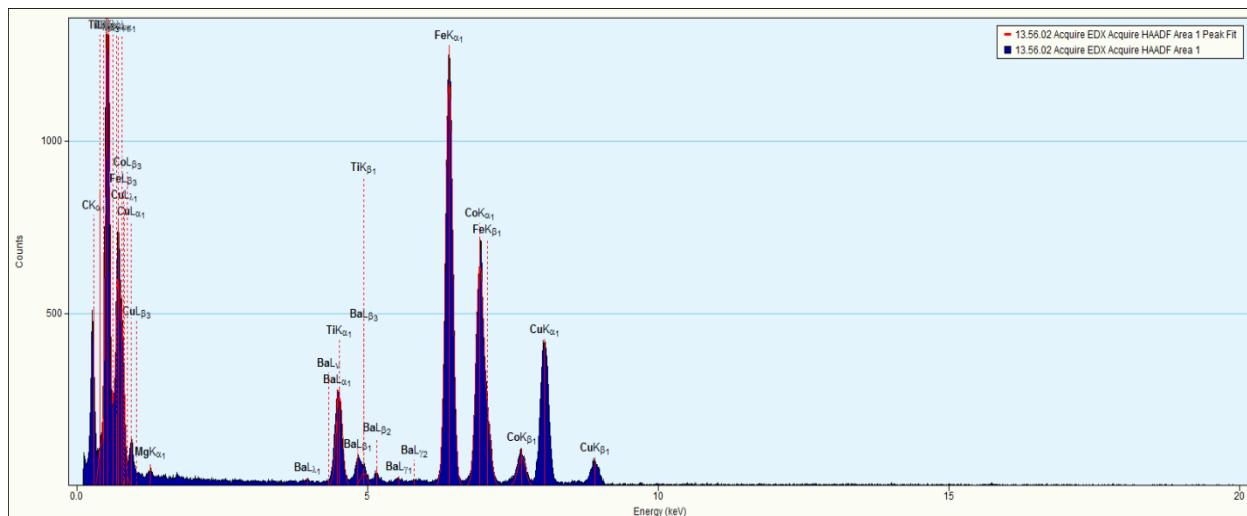
Figure 40. Quantificationofthe EDXS area scan within the yellow frame **of the sample having 1:1 molar ratio**

Distribution of Fe, Co, Ba, Ti and O within FeCoO$_x$-BaTiO$_y$ nanoparticle assembly.

Here, maps of distribution of the denoted elements are represented. More precisely, HAADF-STEM image and EDXS maps of Fe (Fe-K$_\alpha$ line - red), Co (Co-K$_\alpha$ line - green), Ba (Ba-K$_\alpha$ line - blue), Ti (Ti-K$_\alpha$ line - orange) and O (O-K$_\alpha$ line - lavender) distributions are represented on the picture below.
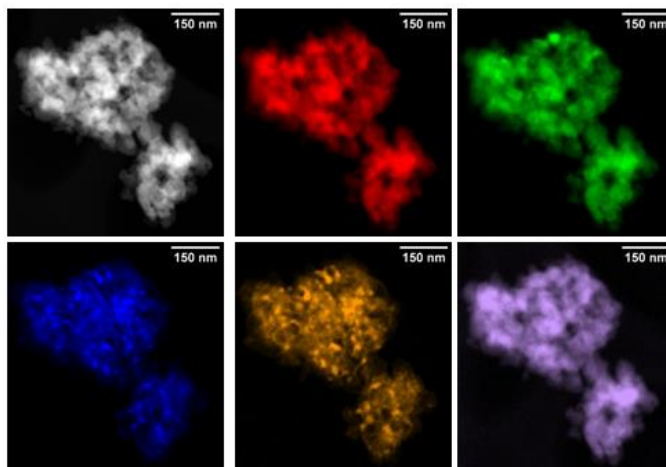
Figure 41. EDXS elemental maps of Fe (Fe-K$_\alpha$ line - red), Co (Co-K$_\alpha$ line - green), Ba (Ba-K$_\alpha$ line - blue), Ti (Ti-K$_\alpha$ line - orange) and O (O-K$_\alpha$ line - lavender) distributions

EDXS map of O together with EDXS maps of Fe-Co and Ba-Ti demonstrate the formation of CoO_z, $FeCoO_x$ and $BaTiO_y$ nanoparticles, while the EDXS elemental map of Fe-Ba shows that no $FeCoO_x$-$BaTiO_3$ core-shell particles are formed. Instead, $BaTiO_3$ particles are located at boundaries of $CoFeO_x$ particles. Therefore, the magnetoelectric coupling has also been achieved with this specific molar ratio.
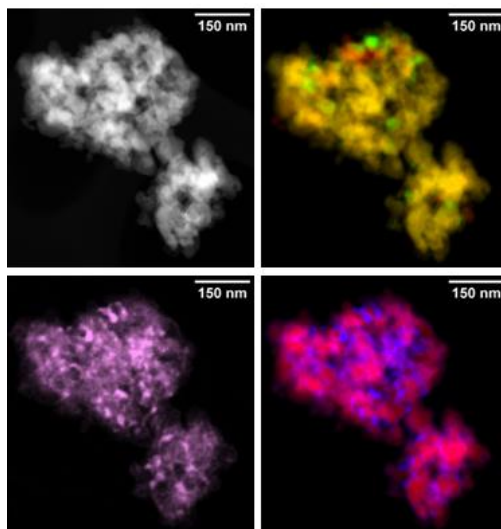
Figure 42. HAADF-STEM image and EDXS maps of Fe – Co, Ba – Ti and Fe – Ba distributions

From the TEM investigations, it can be concluded that BT-CFO nanoparticles were successfully obtained by the proposed sol gel synthesis. Regardless of no core shell formation between them, BT nanoparticles are in the direct contact with CFO nanoparticles and desired magnetoelectric coupling is achieved. To improve the existing nanoparticles, following ideas can be considered:

- Decrease the time of sintering
- Different amount of stearic acid could be used
- Different gelling agent, such as NH_4OH
- Different synthesis, such as Plasma Spark Sintering.

4.3 XRD

In this part of work, crystalline structure of the nanoparticles will be investigated. To obtain these results, XRD was used. Composition was again confirmed by this technique. The following results can be reported:

CFO commercial nanoparticles
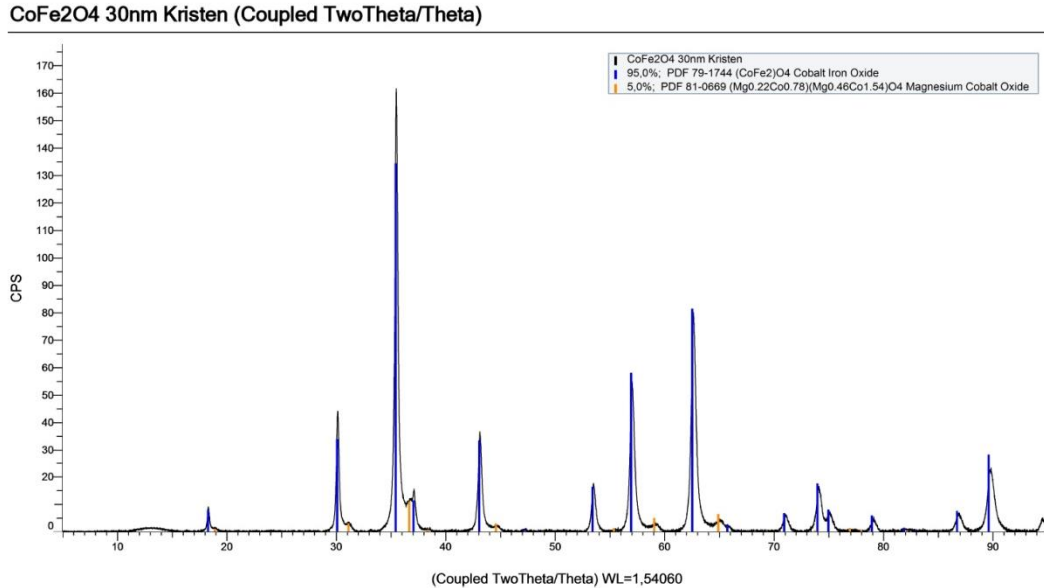
Figure 43. Diffractogram of CFO commercial nanoparticles

In figure 43, diffractogram of the CFO commercial nanoparticles is showed. The obtain peaks correspond to the 2Ө values of the cubic spinel structure. **[48]** Additionally, broadening of the peaks can give a rough estimation if the powder is monocrystalline or polycrystalline. Polycrystalline powders show peak broadening. In this case, peaks are pretty narrow and the powder can be characterized as a monocrystalline cubic spinel cobalt ferrite. However, it can also be noticed that not only cobalt ferrite crystallized. At the same time, magnesium cobalt oxide was formed which is an undesirable component. Since it is present in 5 mass% only, it can be considered as an impurity.

CFO-BT nanoparticles with 2-methoxy ethanol as a gelling agent
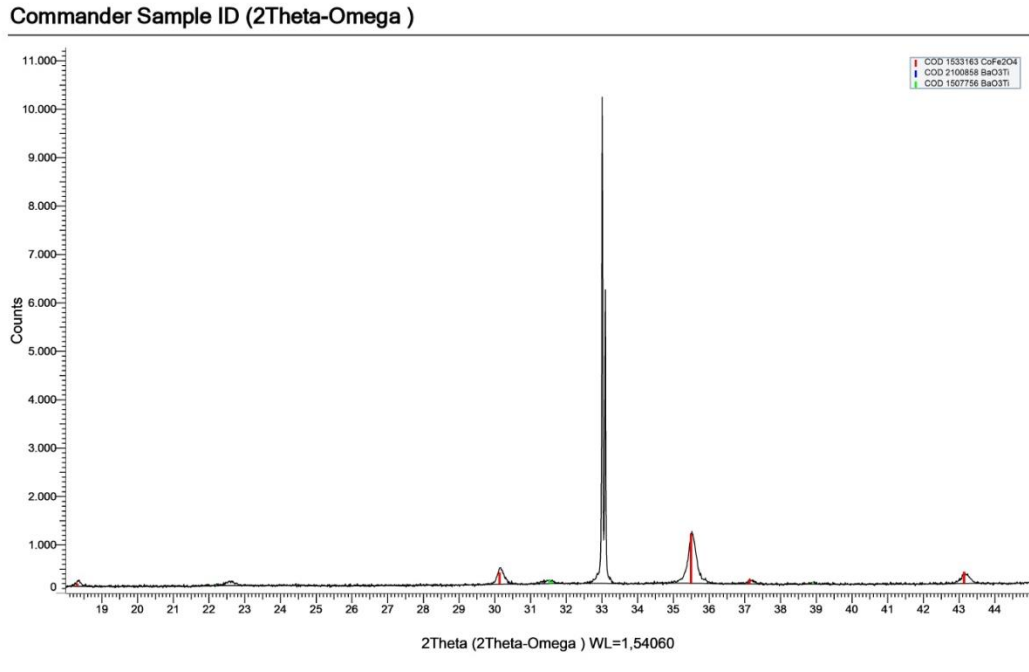
Figure 44. Diffractogram obtained from CFO-BT nanoparticles obtained with 2-methoxy ethanol as a gelling agent

The above diffractogram (Figure 44) was obtained from the composite nanoparticles when 2-methoxy ethanol was used as a gelling agent. The low number of the obtained peeks could be due to the fact that the low amount of the nanoparticles was put on the Si wafer. Nevertheless, XRD confirmed that both CFO and BT crystallized. The peaks which correspond to CFO (red peaks) confirm that CFO crystallized in a cubic spinel structure. Also, some peak broadening can be observed and polycrystallinity can be connected to that. Having polycrystalline nanoparticles is desired, due to the fact that larger number of interfaces results to a better coupling. Additionally, two peaks of barium titanate are observed. One at $2\Theta=31.5^o$ and 33° respectively. The peak (green) at $\Theta=31.5^o$ confirms that tetragonal BT was obtained. However, the proximity of Si wafer (111) peak and BT peak can lead to confusions due to their overlapping.

CFO-BT nanoparticles obtained with citric acid as a gelling agent
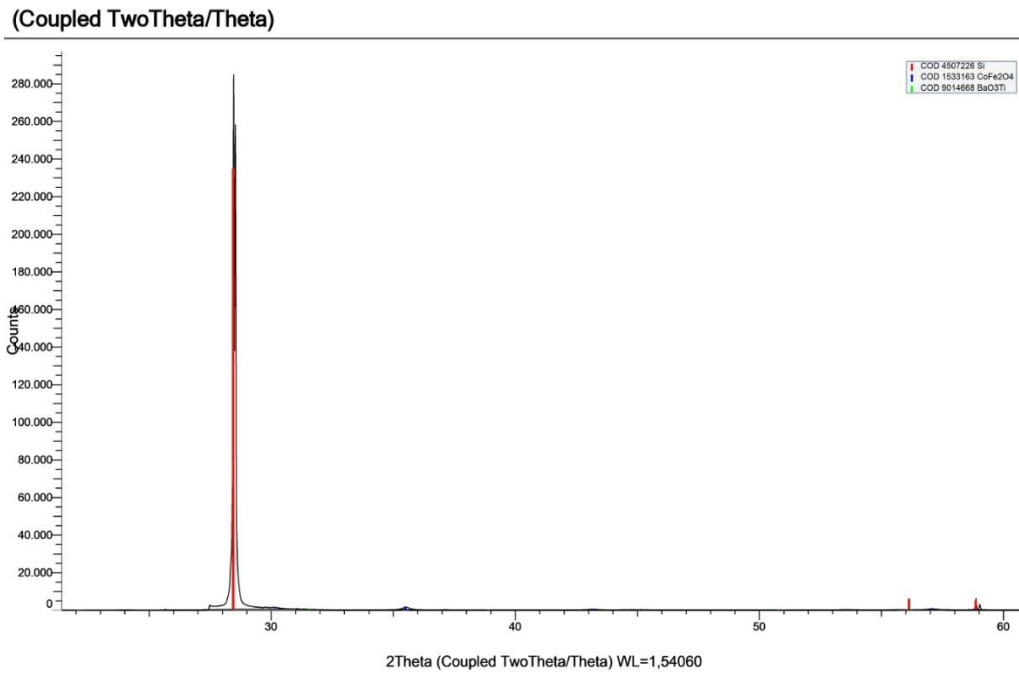
Figure 45. Diffractogram of CFO-BT nanoparticles obtained with citric acid

The above diffractogram (figure 45) is obtained from the synthesis where citric acid was a gelling agent. Correlating the obtained peaks with their corresponding 2Ө values, it can be confirmed that CFO (blue peaks) and BT (green peaks) crystallized. At the same time, an overlap between hexagonal BT and Si wafer peaks is observed. This implies that the use of (100) Si wafer should be avoided when characterization of BT particles is performed. BT crystallized in the hexagonal space group which is not perovskite. Hexagonal BT is characterized by a lower dielectric constant with respect to the tetragonal perovskite BT and unfortunately it is not piezoelectric. However, hexagonal BT is characterized by a larger magnetoelectric effect with respect to the tetragonal BT. **[49]** Furthermore, the peak at around 2Ө=35.5° confirms that CFO crystallized in the inverse spinel structure as desired. However, it can be noticed that only few peaks appeared in spectra. This can be due to the fact that the angular increment was too large or due to the insufficient amount of nanopowder on the Si wafer.

4.4 FTIR

Fourier transform infrared spectroscopy (FTIR) is another technique to confirm the composition of the obtained powders. For the characterization, as previously stated, Bruker Hyperion 27 was used. Report and detailed explanation of the results is given in this section. In all the graphs, absorbance was represented as a function of the wavenumber. The obtained results are the following:

Commercial cobalt ferrite nanoparticles
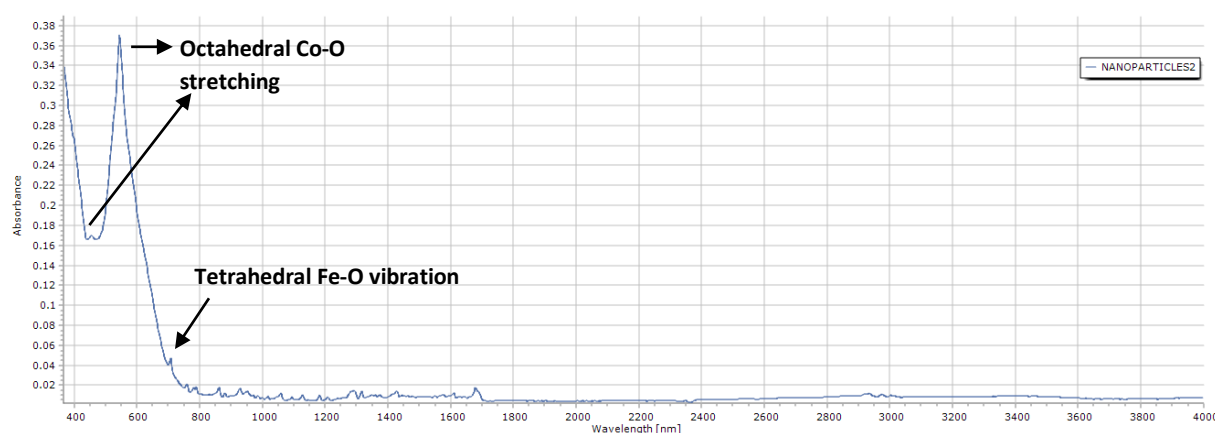
Figure 46. FTIR image of CFO commercial nanoparticles

On the figure above, FTIR spectra of CFO commercial nanoparticles is shown. Recalling the structure of cobalt ferrite, octahedral sites are occupied by Co^{2+} ions, while Fe^{3+} ions either occupy octahedral or tetrahedral sites. The absorbance peak at around 650 cm^{-1} corresponds to the tetrahedral vibration mode between iron and oxygen. However, strong peaks at around 550 cm^{-1} and 400 cm^{-1} correspond to octahedral Co-O stretching that confirms the spinel structure of the CFO nanoparticles. **[50]**

CFO-BT nanopowders
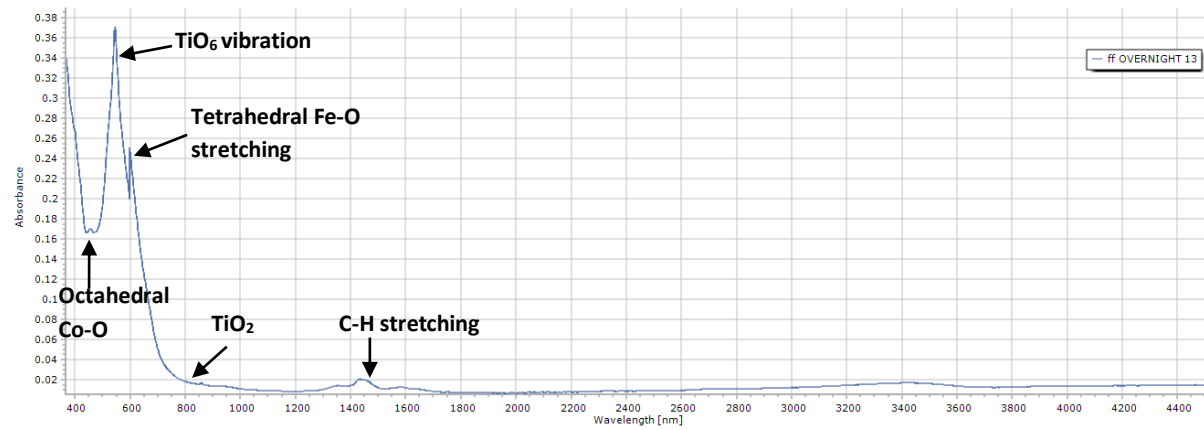
Figure 47. FTIR spectra of the nanopowders obtained with citric acid

The above figure represents FTIR spectra of CFO-BT nanopowders. Characteristic peaks at around, 1450 cm^1, 850 cm^{-1}, 650 cm^{-1}, 550 cm^{-1} and 450 cm^{-1} can be noticed. The broad peak at 1450 cm^{-1} is due to the C-H stretching and it can be described as a low intensity broad band. Very low intensity peak can be observed at 850 cm^{-1} that confirms the small presence of TiO_2. As previously denoted, the vibrational peak at 650 cm^{-1} corresponds to the tetrahedral stretching between iron and oxygen. The characteristic peak at 550 cm^{-1} can be assigned to TiO_6 stretching vibration, which confirms that the octahedral TiO_6 was formed. At the same time, it confirms that the octahedral TiO_6 is bounded to barium. The peak that corresponds to the wavenumber of 450 cm^{-1} confirms the spinel structure of the CFO as discussed before. **[51]**

4.5 Magnetic measurements

Due to the fact that the whole research has been dealt with magnetoelectric nanoparticles, it was essential to perform magnetic measurements. The measurement has been done on the alternating gradient magnetometer (AGM). It has been proved that higher are the coercivity and magnetic saturation, better is the magnetostriction. However, very high coercivityand remanent magnetization lead to the formation of the permanent magnets, which is not desirable. Being on the nanoscale, coercivity will not be so high to form a permanent magnet.Also, it is not desirable for the remanent magnetization to be too low because the particles should still stay magnetized when the application of the field is stopped. The obtained results are represented in the following tables (Table 2 and Table 3) and later on explained.

Table 2. Summary of the key parameters of the respective sample obtained by the AGM measurement

Sample	Coercivity, Hc kA/m	Remanentmagnetization, Mr Am²/kg	Magnetic saturation, Ms Am²/kg
1 (D1)	72.11	5.47	11.34
2 (S1)	91.43	7.067	13.65
3 (K1)	73.74	2.472	4.897
4 (H1)	83.71	9.367	18.36

To get a better insight about previously labeled samples 1-4, explanation is given in the following table.

Table 3. Representation of the measured samples and their brief description

Sample	Description
1	1:1 CFO-BT molar ratio
2	CFO-BT nanoparticles with citric acid as a gelling agent sintered for 1h
3	CFO-BT nanoparticles with 2-methoxy ethanol as a gelling agent
4	CFO-BT nanoparticles with citric acid as a gelling agent sintered for 30 minutes

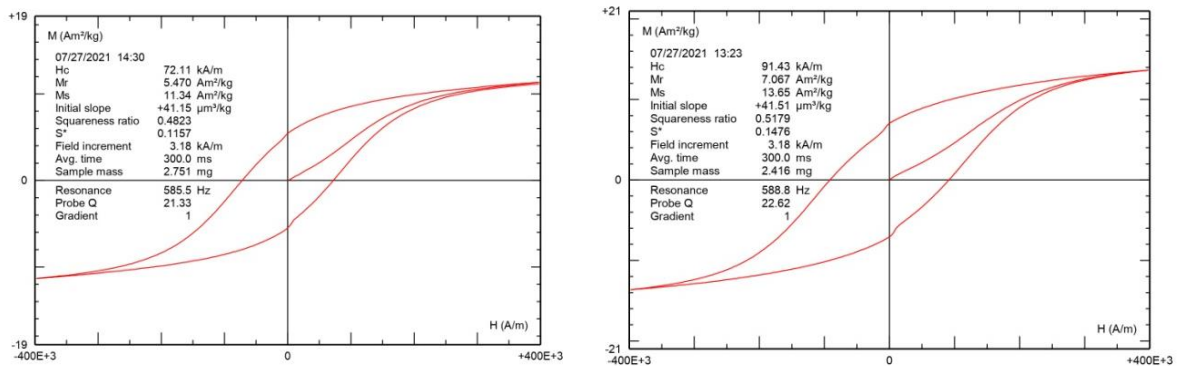The obtained magnetic hysteresis loops are depicted below.

Figure 48. Magnetic hysteresis loops of the sample 1 (left) and the sample 2 (right)
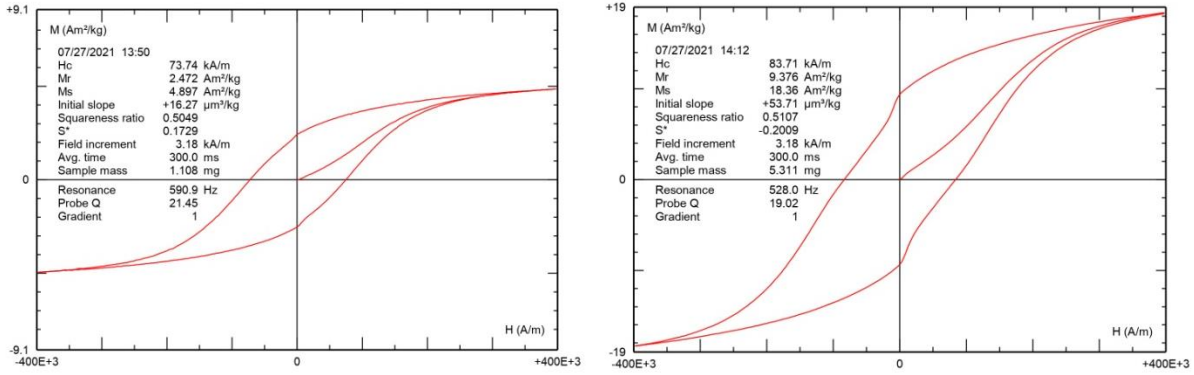
Figure 49. Magnetic hysteresis loops of the sample 3 (left) and the sample 4 (right)

From all the magnetic hysteresis loops (Figure 48 and Figure 49), it can be noticed that the non-linear magnetic behavior is exhibited, hence ferromagnetic particles are obtained. From the recorded values, highest magnetic saturation and remanent magnetization are occurring in the sample 4, meaning that among all the samples, this one reassembles permanent magnet the most. To prepare this sample, calcinations was shortened to half an hour, meaning that lower is the calcinations time, higher will be the magnetic saturation and remanent magnetization.

The lowest values of remanent magnetization and magnetic saturation are achieved in the sample 3, where gellation was achieved by 2-methoxy ethanol. Coercivity values are somewhat the same as in the case of the samples 1, 2 and 4 where gellation was achieved exclusively by the citric acid. Additionally, values of coercivity in the case of all the samples are relatively low to reassemble the permanent magnet behavior. Furthermore, comparing the sample 2 to sample 4, it can be observed that the shorter time of sintering leads to higher values of magnetic saturation and remanent magnetization, hence improved ferromagnetic behavior. Finally, comparing the results obtained with 2-methoxy ethanol and citric acid as a gelling agent,it is clear that in the case of the citric acid, coercivity, magnetic saturation and remanent magnetization are higher. Even if the values are still in the same order in the case of all the samples, it can be concluded that better ferromagnetic performance is achieved in the case of the nanopowders obtained with the citric acid as a gelling agent.

4.5 Cytotoxicity measurements

In this research, injectable magnetoelectric nanoelectrodes have been researched and synthesized. Obviously, a fundamental step is be to measure their toxicity due to their potential use in the human body. Generally, ceramics are inert and in the case of the contact with the human body, no chemical interactions occur. Nevertheless, to be sure, cytotoxicity will be evaluated using different concentration of nanoparticles in water. The following results are reported:
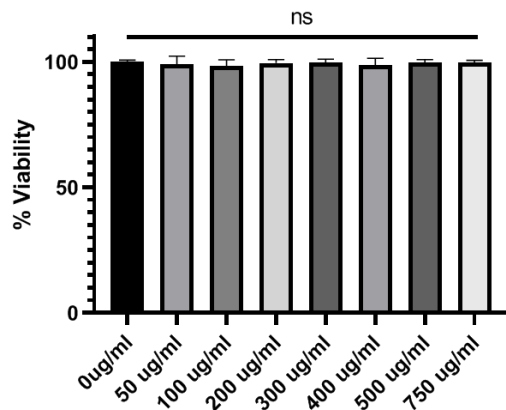
Figure 50. Viability assessment of the nanopowders

Cell viability assessment is used to determine the potential toxicity of the synthesized nanopowders. Viability can be defined as a lifetime measurement of the cell. Moreover, viability ranges from 0 to 100% and it is calculated as a ratio of cells that survived with respect to the total number of cells. Therefore, 0% viability stands for high toxicity and 100% for non-toxic conditions. **[52]** From the picture, as previously denoted, different concentrations of nanoparticles in water are investigated. Also, it can be observed that the toxicity assessment of all the concentrations was more or less the same, being almost 100%. Therefore, it can be concluded that the produced nanopowders are not toxic which was definitely a desired outcome.

5. Conclusions

The aim of this master thesis was to synthesize composite magnetoelectric nanoparticles based on cobalt ferrite and barium titanate that are promising candidates for the applications in the field of neuromodulation. The chosen technique to obtain these powders on a nanoscale was a sol gel synthesis due to its low cost and not complicated management. As precursors of cobalt ferrite, already commercial particles with an average diameter of 30 nm were utilized in the form of ferrofluid where their surface was modified with the oleic acid in order to make them hydrophobic. Barium titanate was prepared from sol and the final powders were obtained by drying and calcinations. To exhibit gellation, hence interconnection and a consequent drop of viscosity, two different gelling agents were used. It was observed that 2-methoxy ethanol didn't provoke a drop of viscosity. Therefore, in this case, solvents were completely dried and the obtained powders calcined. In the case of a citric acid as a gelling agent, a significant drop of viscosity occurred and the gels were separated from the aqueous phase by centrifugation. Later

on, powders were dried, calcined and fully characterized by the mentioned techniques. In the results and discussion section, it was definitely confirmed that the nanoscale powders were successfully obtained. Moreover, SEM showed better results when each step of the reaction was performed for longer than half an hour and that agglomerated particles were obtained which is very often happening in the case of magnetic particles, especially obtained by the sol gel technique. This issue can be solved by the use of mortar and pestle. To get an insight about the elemental composition, EDS analysis was performed. Moreover, it was confirmed that Co, Fe, Ba, Ti and O are present in the powders. By TEM, more detailed information about the particles' morphology was gained and the composition was confirmed. Apart from the confirmation of the formed compounds, distributions of Co, Fe, O, Ba and Ti were given. Moreover, it was proved that shortening the calcinations times, will have a good impact on the particle's size and that particles having lower diameters were obtained when the calcinations time was shorter. Additionally, it was observed that cobalt ferrite and barium titanate particles were in the direct contact sharing interfaces meaning that the coupling among them was achieved. Also, nanoparticles obtained with molar ratio of CFO:BT=1:1 was investigated and unfortunately, the $CoFe_2O_3$ nanoparticles were obtained. Another technique used to confirm the structure and composition of the nanoparticles was FTIR were the obtained peaks confirmed that cobalt ferrite crystallized in the form of a desired inverse spinel structure and that BT had a perovskite structure. Therefore, the obtained particles show a multiferroic behavior. With XRD, again, the structure of these nanopowders was confirmed despite an issue of an insufficient amount of powders on the Si wafer. Finally, magnetic measurements were performed and it was reported that the particles were ferromagnetic and that in the case of the citric acid as a gelling agent, higher magnetic saturation and higher remanent magnetization were achieved than in the case when 2-methoxy ethanol was used for gellation.

Even better magnetoelectric coupling can be achieved in the form of core-shell nanoparticles, which will be definitely more investigated in my future research.

6. Bibliography

[1] Krames, Peckham, and Rezai (eds) *Neuromodulation v.1-2,* (2009)

[2] K.L. Kozielski, A. Jahanshahi, H.B. Gilbert, Y.Yu, Ö. Erin, D. Francisco, F. Alosaimi, Y. Temel, M. Sitti, Nonresonant powering of injectable nanoelectrodes enables wireless deep brain stimulation in freely moving mice. *Science Advances 7* (2021)

[3] S. K. Karan, R. Sriramdas, M-G Kang, Y. Yan, S. Priya, Small-Scale Energy Harvesting Devices for Smart Electronics. *Encyclopedia of Materials: Technical Ceramics and Glasses 3,* 391-425 (2021)

[4] C. Schmitz-Antoniak, H. Trivedi, A. S. Nazrabi, V. V. Shvartsman, Magnetoelectric coupling on multiferroic cobalt ferrite-barium titanate ceramic composites with different connectivity schemes. *ActaMaterialia*(2015)

[5] S. Datta, Piezoelectric Materials: Crystal Orientation and Poling direction. *COMSOL blog* (2014)

[6] A. Mayeen, N. Kalarikkal, Development of ceramic controlled piezoelectric devices for biomedical applications. *Fundamental biomaterials: Ceramics* (2018)

[7] K. C. Kao, Electric Polarization and Relaxation, *Dielectric phenomena in Solids*, 41-114 (2014)

[8] D. Damjanovic, Hysteresis in Piezoelectric and Ferroelectric Materials, *The Science of Hysteresis 3, Elsevier* (2014)

[9] Ferroelectric Dielectric Hysteresis and Hysteresis Loop, *Practical Electron Microscopy and Database – an online book*

[10] M. Sajjia, A. Baroutaji, M. Hasanuzzaman, A.G. Olabi, Magnetostrictive Cobalt Ferrite Nanoparticles Preparation and Magnetic Characterization, *Reference Module in Materials Science and Materials Engineering* (2016)

[11] S. Vinogradov, A. Cobb, G. Light, Review of magnetostrictive transducers (MsT) utilizing reversed Wiedemann effect, *AIP Conference Proceedings 1806, 020008* (2017)

[12] D. Davino, Magnetostrictive Actuators, *Reference Module in Materials Science and Materials Engineering* (2020)

[13] H. E. Burke, Magnetostriction, *Handbook of Magnetic Phenomena,* 253-270 (1986)

[14]Types of Magnetism – definitions, retrieved from https://material-properties.org/types-of-magnetism-definition/

[15] R. Nistico, F. Cesano, F. Garello, Magnetic Materials and Systems: Domain Structure Visualization and Other Characterization Techniques for the Application in the Material Science and Biomedicine, *Inorganics* (2020)

[16]Magnetostriction (2021) retrieved from https://eng.libretexts.org/@go/page/335

[17]Magnetism, retrieved from http://depts.washington.edu/mictech/optics/sensors/week2.pdf

[18] Physics of Nondestructive Evaluation, Ferromagnetic materials, retrieved from https://www.nde-ed.org/Physics/Magnetism/magneticdomain.xhtml

[19]Muljadi, P. Sardjono, Suprapedi, Preparation and characterization of 5 wt% epoxy resin bonded magnet NdFeB for micro generator application, *2nd International Conference on Sustainable Energy Engineering and Application,* ICSEEA (2014)

[20] M. Fantauzzi, F. Secci, M. S. Angotzi, C. Passiu, C. Cannas, A. Rossi, Nanostructured spinel cobalt ferrites: Fe and Co chemical state, cation distribution and size effects by X-Ray Photoelectron Spectroscopy, *RSC Advances 33* (2019)

[21] X. Zeng, J. Zhang, S. Zhu, X. Deng, M. Hongbin, J. Zhang, Q. Zhang, P. Li, D. Xue, N. Mellors, X. Zhang, Y. Peng, Direct observation of cation distributions of ideal inverse spinel $CoFe_2O_4$ nanofibers and correlated magnetic properties, *Nanoscale 9* (2017)

[22] K. Mohaindeen, P. A. Joy, High magnetostriction and coupling coefficient for sintered cobalt ferrite derived from superparamagnetic nanoparticles, *Applied Physics Letter 101, 072405* (2012)

[23] A. Thankappan, N. Kalarikkal, S. Thomas, A. Padinjakkara, Polymeric and Nanostructured Materials: Synthesis, Properties and Advanced Applications (2018)

[24] H-L. Wang, Structure and Dielectric Properties of Perovskite – Barium titanate ($BaTiO_3$), San Jose University (2002)

[25] Barium titanate, retrieved from https://eng.libretexts.org/Bookshelves/Materials_Science/TLP_Library_I/28%3A_Ferroelectric_Materials/28.8%3A_Barium_Titanate

[26] P. Fulay, J-K. Lee, Ferroelectrics, Piezoelectrics and Pyroelectrics, *Electronic, Magnetic and Optical Materials 1st edition* (2010)

[27] Z. Lee, M. Ye, M. Wang, Multifunctional Photocatalytic Materials For Energy, 1st edition (2018)

[28] B. Jiang, J. Iocozzia, L. Zhao, H. Zhang, Y-W. Harn, Y. Cheen, Z. Lin, Barium titanate at the nanoscale: controlled synthesis and dielectric and ferroelectric properties, *Chemical Society Reviews* (2019)

[29] F. S. Samghabadi, L. Chang, M. Khodadadi, K. S. Martirosyan, D. Litvinov, Scalable, cost – efficient synthesis and properties optimization of magnetoelectric cobalt ferrite/barium titanate composites, *APL Materials 9,* 021104 (2021)

[30] Under the microscope: Key differences between SEM and Optical microscope, retrieved from https://www.atascientific.com.au/microscope-key-differences-sem-optical-microscopy/)

[31] What is SEM? Scanning electron microscope explained, Thermofisher scientific retrieved from https://www.thermofisher.com/blog/microscopy/what-is-sem-scanning-electron-microscopy-explained/

[32] I. Perissi, Study of Ionic Liquids as innovative fluids in Material Science applications (2009)

[33] A. Nanakoudis, SEM: Types of Electrons and Information They Provide, *ThermoFischer Scientific* (2019)

[34] N. Gleichmann, SEM vs TEM, retrieved from - https://www.technologynetworks.com/analysis/articles/sem-vs-tem-331262

[35] F. Makobi, Transmission Electron Microscope (TEM) (2019)

[36] Basic principles of transmission electron microscope, retrieved from http://www.hk-phy.org/atomic_world/tem/tem02_e.html

[37] What is X-Ray Diffraction Analysis (XRD) and How Does It Work?, retrieved from https://www.twi-global.com/technical-knowledge/faqs/x-ray-diffraction

[38] D. Malacara, Interference, *Methods in Experimental Physics vol 26,* 1-48 (1989)

[39] Bragg's law of diffraction, ETH Zurich, retrieved from https://www.microscopy.ethz.ch/bragg.htm

[40] Bruker's guide to Infrared Spectroscopy, retrieved from https://www.bruker.com/it/products-and-solutions/infrared-and-raman/ft-ir-routine-spectrometer/what-is-ft-ir-spectroscopy.html

[41] J. M. Cameron, C. Bruno, D. R. Parachalil, M. J. Baker, F. Bonnier, H. J. Butler, H. J. Byrne, Vibrational spectroscopic analysis and quantification of proteins in human blood plasma and serum, *Vibrational Spectroscopy in Protein Research – from Purified Proteins to Aggregates and Assamblies,* 269-314 (2020)

[42] A. Winter, Organic Chemistry I, 2nd edition ,9781119293378 (2014)

[43] Total Internal Reflection, Mini Physics, retrieved from https://www.miniphysics.com/total-internal-reflection-2.html

[44] Evanescent Waves, *RP Photonics Encyclopedia,* retrieved from https://www.rp-photonics.com/evanescent_waves.html

[45]CyQUANT™ LDH Cytotoxicity Assay Kit, C230300 and C20301, *ThermoFischer Scientific*

[46] R. A. Harris, P. M. Shumbula, H. van der Walt, Analysis of the Interaction of Surfactants Oleic Acid and Oleylamine with Iron Oxide Nanoparticles through Molecular Mechanics Modeling, , 31, 13, 3934–3943, *Langmuir* (2015)

[47] V. Corral-Flores, D. Bueno-Basques, R. F. Ziolo, Synthesis and characterization of novel CoFe2O4-BaTiO3 multiferroic core-shell type nanostructures, *ActaMaterialia 58,* 746-769 (2010)

[48] A. Yakubu, Z. Abbas, N. A. Ibrahim, M. Hashim, Effect of Temperature on Structural, Magnetic and Dielectric Properties of Cobalt Ferrite Nanoparticles Prepared via Co-precipitation Method (2015)

[49] N. H. Yusoff, R. A. M. Osman, M. S. Idris, K. N. D. K. Muhsen, N. I. M. Noor, Dielectric and Structural Analysis of Hexagonal and Tetragonal Phase $BaTiO_3$, *AIP Conference Proceedings 2203,* 020038, 1-5 (2020)

[50] S. Akhtar, W. An, X. Niu, K. Li, S. Anwar, K. Maaz, M. Maqbool, L. Gao, Toxicity of PEG-coated CoFe2O4 Nanoparticles with Treatment Effect of Curcumin, *Nanoscale Research Letters* 13, 52 (2018)

[51] R. Ashiri, Detailed FT-IR spectroscopy characterization and thermal analysis of synthesis of barium titanate nanoscale particles through a newly developed process, *Vibrational Spectroscopy,* vol 66, 24-29 (2013)

[52] Synopsis of Cell Proliferation, Metabolic Status, and Cell Death, *Cell Signaling Technology,* retrieved from https://www.cellsignal.com/science-resources/cell-viability-and-survival